ELSEVIER

Coordination Chemistry Reviews 233–234 (2002) 319–339

COORDINATION CHEMISTRY REVIEWS

www.elsevier.com/locate/ccr

# Studies of metal binding reactions in metallothioneins by spectroscopic, molecular biology, and molecular modeling techniques

Jayna Chan, Zuyun Huang, Maureen E. Merrifield, Maria T. Salgado, Martin J. Stillman *

*Department of Chemistry, University of Western Ontario, London, Ont., Canada N6A 5B7*

## Contents

Abstract . . . 319
1. Introduction . . . 320
   1.1 Metallothionein . . . 320
   1.2 Metal clusters in metallothioneins . . . 321
   1.3 The role of cysteines in metallothionein . . . 322
2. Preparation of recombinant metallothionein . . . 323
3. Electrospray ionization mass spectrometry (ESI–MS) . . . 324
   3.1 Recombinant human MTs with S tag in low and neutral pH . . . 324
4. Kinetics of Cu(I) binding to metallothionein . . . 326
5. Scanning tunneling microscopy (STM) . . . 328
6. Molecular modeling . . . 331
   6.1 Computational details and construction of the model . . . 331
   6.2 Molecular mechanics . . . 332
      6.2.1 The $Cd_7$–MT2A structure . . . 332
      6.2.2 The $Zn_7$–MT2A structure . . . 333
   6.3 Molecular dynamics simulation . . . 334
Acknowledgements . . . 337
References . . . 339

## Abstract

Metallothioneins (MTs) are a class of metal-binding proteins characterized by a high cysteine content (up to 30% of the amino acid residues), low molecular weight, and lack of aromatic amino acid residues. Remarkable metal-binding properties have been reported both in vivo and in vitro by a number of different analytical techniques. Chemical and spectroscopic studies have shown that an unusually wide range of metals bind to MT. $^{113}Cd$ and $^{1}H$-NMR techniques have been used successfully to determine the structures in a number of different proteins. Together with X-ray diffraction results, analyses of these NMR data have established that in mammalian $Cd_7$–MT and $Zn_7$–MT, the metals are tetrahedrally coordinated in two isolated domains with stoichiometries of $M_4S_{11}$ and $M_3S_9$. Recently, Stillman, collaborators, and coworkers have characterized the Zn(II), Cd(II), Cu(I), Ag(I), Au(I) and Hg(II) containing forms of MTs from mammalian, yeast, and recombinant human sources using a number of different spectroscopic techniques. Optical spectroscopy, and in particular circular dichroism and luminescence, have provided rich details of a complicated metal binding chemistry, whether metals are added directly to the metal free, apo-MT, or to the Zn-containing protein. Electrospray ionization mass spectrometry is a powerful technique for the characterization of proteins in general directly from solution. For MTs, both from mammalian and recombinant sources, use of this technique allows study of the details of metal binding to the protein as a function of metal loading and pH. Kinetic studies allow determination of the metal binding mechanism when Cu(I) binds to both the metal-free and Zn(II) protein. Scanning tunneling microscopy is a surface analysis technique capable of producing nanoscale images with atomic resolution and is being applied to obtain images of MT on Au(111) surfaces. Molecular modeling, together with

* Corresponding author. Tel.: +1-519-661-3821; fax: +1-519-661-3022
*E-mail address:* martin.stillman@uwo.ca (M.J. Stillman).


PII: S0010-8545(02)00176-5

XANES, XAFS, and structural information from 2D-$^1$H-NMR data allow the determination of 3D structures of a range of MTs. Finally, molecular dynamics (MD) calculations have been carried out to investigate the motion of the metal-containing and metal free peptides, with special interest in the region of the metal binding site.


*Keywords:* Metallothionein (MT); Recombinant protein; Metal-binding protein; Zinc thiolate; Cadmium thiolate; Copper thiolate; Spectroscopy; Electrospray ionization mass spectrometry (ESI–MS); Kinetics; Scanning tunnelling microscopy (STM); Molecular modeling; Molecular dynamics; Protein folding

## 1. Introduction

Proteins are considered the building blocks of life because of their involvement in a diverse assortment of biological processes that occur in living cells, ranging from structural to enzymatic roles. The wide range of functions that proteins undertake is defined by both their structural conformations and their chemically active sites. In general, it is only after a polypeptide chain has folded into its final conformation that it is capable of carrying out its specific functions. The folding process is in general driven by a number forces, including hydrogen bonding, disulfide cross-linking, simple steric interactions between specific amino acid side chains, and hydrophobic effects [1]. However, in metalloproteins, metal ions may also facilitate protein folding by providing internal cross-links that directly lead to the final conformational state. DNA-binding proteins, for example, contain metalloprotein structures that consist of 25–60 amino acid residues arranged around one or two $Zn^{2+}$ ions [2–4]. These metal ions are tetrahedrally coordinated to the side chains of the amino acids cys, his, and, occasionally, asp or glu. The coordination to $Zn^{2+}$ allows the protein to fold into a compact, stable conformation that can then interact with nucleic acids [2–4]. Metal ions such as $Fe^{2+}$, $Fe^{3+}$, $Zn^{2+}$, $Cu^{2+}$ and $Cu^{+}$ are incorporated into biological systems as key structural and/or functional elements in many enzymes that control processes that are required for optimal growth and development of organisms [5,6].

Nearly one-third of all known enzymes require the presence of metal ions as cofactors for catalytic activity [7], with seven out of the ten biologically essential transition metals using sulfur coordination in some or all of their biological manifestations [8]. These metal ions are essential for the catalysis of many vital biological activities including electron transfer, oxygen binding, sulfite and nitrite reduction, hydrolysis, and dehydrogenation reactions [6].

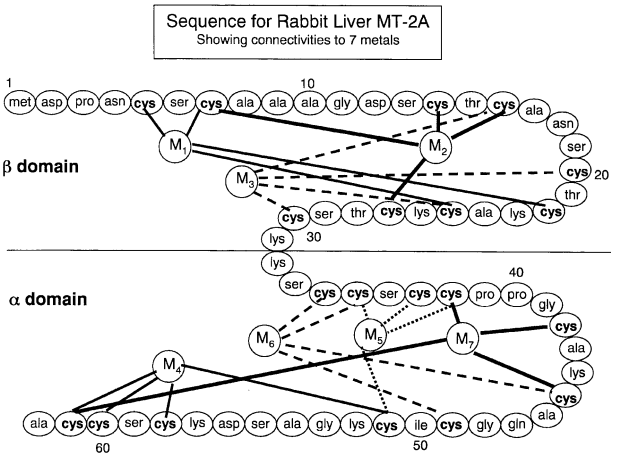


Fig. 1. Primary amino acid sequence for rabbit liver MT2A based on the sequence reported by Kagi [10]. The 20 cysteine residues (Cys) are shown in bold. The β domain is located at the N-terminal of the protein and consists of residues 1–31, while the α domain is located at the C-terminal and consists of residues 32–62.

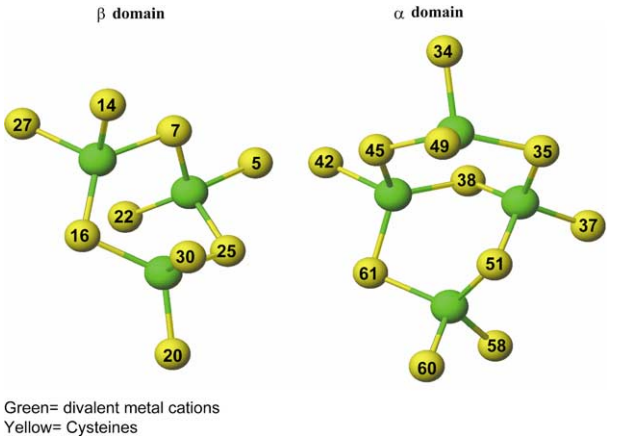


Fig. 2. Metal–thiolate cores for Cd(II) and Zn(II) in β and α domains of mammalian MT based on the connectivities from NMR and X-ray [35,36]. This diagram is from the calculation reported by Fowle et al. [27] with modification that includes use of force field for both terminal and bridging thiolate sulfurs [100]. The modified bond lengths and angles are listed in Tables 3–7 in Section 6 (reproduced with permission from Fowle et al. [27]).

### 1.1. Metallothionein

One class of metalloprotein of great current interest are the metallothioneins (MTs). Mammalian MT proteins (for example, rabbit liver MT, Figs. 1 and 2) are low molecular weight proteins (60–62 amino acid residues for mammalian protein; with a molar mass of ca. 6000–7000 Da) [9–15] that are characterized by their high cysteine content (up to 30% residues). Their affinity for binding a very wide range of transition-metal ions (especially, metals from Groups 11 and 12) has made the MT class of proteins interesting from both biochemical

and inorganic points of view [16]. The initial discovery of MT was in 1957 by Margoshes and Vallee [17] during a study designed to identify the metal-binding protein responsible for the natural accumulation of cadmium within equine kidney cortex [9]. Since their discovery, MTs are still the only known biological compounds to contain cadmium naturally [16]. MTs are found ubiquitously in mammals, crustaceans, and some unicellular species, often as multiple isoforms within these systems [18,19].

The fundamental function of MTs within these living systems has not yet been determined [16] although there are several hypotheses, including:

1) Acting as metallochaperones to transport metal ions to other proteins (i.e. zinc finger proteins, which are important DNA-binding, regulatory proteins) [20].
2) Controlling the concentrations of free ion concentrations of the essential trace elements zinc and copper [21].
3) Providing storage and supply management.
4) Acting as detoxification agents of heavy metals (i.e. cadmium and mercury) [18].
5) Providing a protective role in sequestering heavy metals [22,23].
6) Protection from a variety of stress conditions [21].

There is also strong evidence that many species of mammals have high endogenous hepatic levels of zinc and copper bound MT in fetal and early neonatal life, which suggests that MT may act as an intracellular storage protein for these essential metals during perinatal development [24]. It has been proposed that high levels of MT can be present in tissues that are undergoing rapid growth and development, in order to supply zinc and copper for nucleic acid metabolism, protein synthesis, and other metabolic processes [6]. The biochemical properties of a range of MTs have been reviewed in a number of monographs [14,25,26].

### 1.2. Metal clusters in metallothioneins

Naturally occurring mammalian MTs are typically isolated as fully metallated species with zinc(II) or copper(I). Cadmium-containing protein is also isolated when exposure to cadmium has occurred, which might take place from cadmium-rich feed or water. The tertiary structure of the mammalian protein consists of two domains attached by a short linker sequence, resulting in a dumbbell-shaped appearance (see Fig. 12 below). MTs are unique amongst metalloproteins in the number of different metals they can bind both in vivo and in vitro. Metal ions as diverse as Zn(II), Cd(II), and Hg(II), and Cu(I), Ag(I), and Au(I) (Groups 11 and 12 metal ions) are bound solely through bridging and terminal thiolate groups of the cysteines, no interactions with other amino acids have been documented [14,27,28]. Indeed, a recurring feature of the MTs isolated from the range of sources is the close homology between sequences of cysteine residues with the groupings of cys–cys, cys–X–cys, and cys–X–Y–cys (where the X and Y are amino acids other than cys). These grouping naturally provide the chelation necessary to bind the metal ions (see Figs. 1, 2 and 4 and Table 1). The formation of these specific coordination geometries requires the polypeptide chain to wrap tightly around the metal ions, forming highly organized metal–thiolate clusters shown in Fig. 2 for the formation of the tetrahedrally-coordinated Zn(II) and Cd(II), and Fig. 3 for the trigonally-coordinated Cu(I) and Ag(I) [9–14,28–31]. The three-dimensional structures formed by the binding of metals does not only depend on the metal bound, but also on the number of metals bound to the protein, and the coordination preference of the metal, tetrahedral, trigonal or digonal.

As of today, the structural chemistry of MT comes largely from NMR studies (both metal-dependent and 2-dimensional $^{1}$H-NMR) [32,33,35], X-ray diffraction [34–36], and X-ray absorption spectroscopy [14,37–40], that together provide the detailed metal–sulfur bond length information and metal–thiolate connectivity data to allow a number of structures to be proposed [27,28]. While X-ray crystallography has helped solve the three-dimensional structure of many proteins, only one structure of a MT has been reported; that of rat liver Cd, Zn–MT by Stout and coworkers [34–36].

The basis of the folding mechanism for MTs is the formation of metal–thiolate bonds that form native clusters that subsequently define a specific three-dimensional structure (see Figs. 2 and 3) [27,28,35–40]. Metallation reactions from metal-free MT (apo-MT) and metal substitution reactions in $Zn_7$–MT can provide data with which to map the sequence of events required for this unique protein folding mechanism. The mechanism by which a polypeptide chain folds to reach its native and functional structure has remained an intriguing problem of fundamental interest [37–41].

Following coordination of tetrahedral-directing divalent metal ions such as Cd(II) and Zn(II) [14,15] to the protein's reduced form, the cysteinyl thiol groups coordinate to the metals to form the following metal–thiolate clusters in the mammalian protein [14,27] (Fig. 2):

1) $M(II)_3S_9$ in the N-terminal, named the β domain.
2) $M(II)_4S_{11}$ in the C-terminal, named the α domain.

Where M represents the bound metal and S represents the cysteinyl sulfur.

Coordination can also occur with digonal- and trigonal-directing metal ions such as Cu(I), Au(I) and

Table 1
Amino acid sequences and masses of recombinant and rabbit liver MTs (data from ref. [69])

| Recombinant amino acid sequence | | Metal-free + S-tag | | Cd-binding + S-tag | |
|---|---|---|---|---|---|
| | | Theoretical mass (amu) | Mass from ESI–MS (amu) | Theoretical mass (amu) | Mass from ESI–MS (amu) |
| s-peptide tag | MKETAAAKFERQHMDPDLGTLVPRGS | | | | |
| β | MGKAAAACSCATGGSCTCTGSCKCKEC-KCNSCKKAAAA | 6564.7 | 6564.5 | 6896.9 | 6895.5 |
| α | MGKAAAACCSCCPMSCAKCAQGCV-CKGASEKCSCCKKAAAA | 6894.3 | 6894.3 | 7335.9 | 7336.5 |
| βα | MGKAAAACSCATGGSCTCTGSCKCKEC-KCNSCKKAAAACCSCCPMSCAKCAQGC-VCKGASEKCSCCKKAAAA | 9884.8 | 9886.5 | 10657.6 | 10659.8 |
| Rabbit | | Metal-free | | $Cd_7$-binding | |
| | | Theoretical mass (amu) | Mass from ESI–MS (amu) | Theoretical mass (amu) | Mass from ESI–MS (amu) |
| βα | MDPNCSCAAAGDSCTCANSCTCKACKC-TSCKKSCCSCCPPGCAKCAQGCICKGAS-DKCSCCA | 6083.2 | 6083.3 | 6856.0 | 6856.1 |

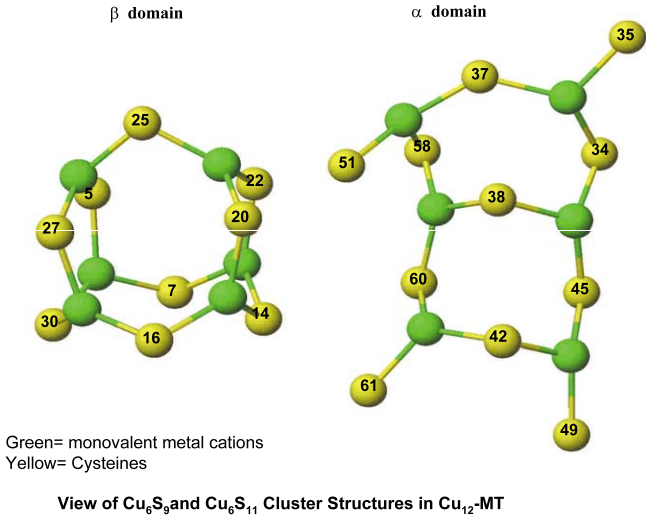


Fig. 3. Metal–thiolate cores for trigonal co-ordination of Cu(I) and Ag(I) by S in β and α domains of mammalian MT based on the connectivities from the calculation of Presta et al. [28] (reproduced with permission from Presta et al. [28]).

Ag(I) [28] (Fig. 3) to form the following clusters in the mammalian protein:

1) $M(I)_6S_9$ in the N-terminal β-domain.
2) $M(I)_6S_{11}$ in the C-terminal α-domain.

Interpretation of absorption, CD, XANES, and EXAFS data suggests that Hg(II) forms a much more complicated series of species, with a series of clusters based on distinct tetrahedral, trigonal and digonal coordinations.

### *1.3. The role of cysteines in metallothionein*

The cysteinyl sulfurs (–SH) act as the sole ligands for the metal ions, forming integrated metal–thiolate clusters that involve the thiolates in both bridging and terminal co-ordination [14,27,28,33]. Highly conserved homology [15] has been found between the different species of MTs in which the amino acid sequences cys–cys, cys–x–cys and cys–x–y–cys (cys = cysteine; x and y are any amino acid except cysteine) are located in similar positions on the sequences [9–15,34–36,42]. The apo protein (no bound metal ions) structure of the MT protein contains cysteine (–SH) in the reduced form and the peptide exists as an essentially random chain [9–15,34–36,42], lacking regions of significant secondary structures, such as α helices or β-pleated sheets. Because the cysteines are very reactive, the sulfur will readily oxidize to form cross-linking disulfide bonds (–S–S–). This significantly changes the metal binding properties as cluster formation is inhibited.

Finally, the lack of aromatic residues [9–15] throughout the MTs allows detailed optical spectroscopic analyses to be carried out. Optical spectroscopic methods such as electronic absorption, circular dichroism, and emission can be employed in order to observe the metal charge transfer transitions that occur between 220 and 350 nm [14,30], a region that would normally be completely masked by the presence of aromatic groups. Such spectroscopic methods, therefore, can be used to characterize and differentiate metallated MTs because the coordinated metals exhibit different spectroscopic properties depending on the metal bound, the co-

ordination geometry adopted, and the peptide wrapping in the region of the metal binding site [9].

One reason that MT has such an intimate connection with metal ion metabolism is that MT expression itself is metal-induced. The gene encoding the MT protein contains the metal responsive element (MRE), a regulatory element that induces protein expression in the presence of metal ions [43]. Though metal ions are one of the major effectors of MT expression, several other inducers exist, including certain hormones, cytokines, growth factors, tumor promoters and many other chemicals, not to mention induction due to physical stress [21].

The importance of the MT proteins is evident in that they appear to play key roles in the regulation of essential metal ions within a vast number of living systems. In order to discern the fundamental function of these proteins, a number of studies have been undertaken in biochemistry to determine the role of MT in metabolism, in genetics, which deals with MT at the DNA level, and in bioinorganic chemistry, which deals with the metal-binding aspect of MT including structure and properties of the proteins.

The Stillman research group at the UWO have been working on aspects of the bioinorganic chemistry of the MTs for many years. The previous work has been reviewed in a number of publications, and we refer the reader to these for summaries of the spectroscopic studies that underpin the work described here [5,12,14,15,25,27,28,37–40,44–69]. In this review, we highlight on-going studies at the University of Western Ontario: first in Section 2 studies are described that concern the synthesis of recombinant peptides with specially designed sequences that will probe the metal binding properties for functional aspects of the structures formed naturally, this is in collaboration with Dr. Peter Kille at Cardiff University, Wales, UK. In Section 3, we describe detailed mass spectroscopic studies using the relatively new technique of electrospray ionization mass spectrometry. These studies began in collaboration with Professor Michael Siu at York University. As can be seen from the data shown here (Fig. 6), there is immense complexity in these spectra as the metal distributions change as a function of both loading and competitive ligands (here protons). Key novel information from the ESI–MS data is the distribution of charged states under different pH and metal-loading conditions. The charge states represent exposed, protonatable sites and, therefore, provide an indication of the folded status of the peptide. Section 4 deals with the reaction mechanisms involved in metallation and demetallation. No mechanism for metallation of MT either in vivo or in vitro has been elucidated to date. Kinetic studies are complicated by the large numbers of metals and potential binding sites that are possible. Our current studies extend work first reported some years ago in which the substitution of 12 Cu(I) for seven Zn(II) could be followed for each Cu(I) added, as the protein binding site clearly changed as each Cu(I) was bound [63]. Section 5 describes initial studies carried out in collaboration with Professor Peter Norton at the UWO to image MTs on gold surfaces. In these preliminary studies, we show here the energy minimized calculation of the protein weakly bound to the gold surface. Finally, we describe in Section 6 recent results from a very extensive series of calculations using molecular modeling and molecular dynamics (MD) techniques to investigate the spatial properties of the peptide and its bound metals [27,28]. In the study shown here we demonstrate how a length of peptide that extends from the N-terminal of the protein wraps around the domains enhancing formation of a more globular structure. But over time, we can see that this structure is fluxional perhaps accounting for the mass estimations from size exclusion chromatography.

## 2. Preparation of recombinant metallothionein

The classic method of producing MT [9–11,21] is by extracting the protein from animal livers and kidneys. Our previous studies have used primarily rabbit liver MT isoform 2A [14,37–40,46–63]. However, recombinant protein expression is an alternative source that has recently been employed that is beneficial in terms of flexibility of production, reduction in the use of animals,

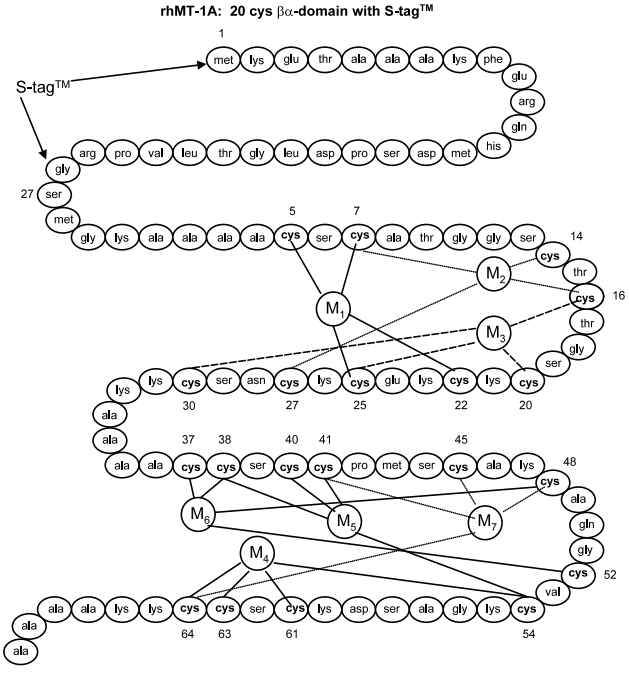


Fig. 4. Amino acid sequence for the recombinant βα human MT1 (rhMT1). The numbers of the cysteines match those of rabbit liver MT2A and are consistent with the numbering scheme shown on the metal–thiolate clusters in Figs. 2 and 3. Note the longer linker region between the β and α domains. Diagram adapted from Stillman et al. [27].

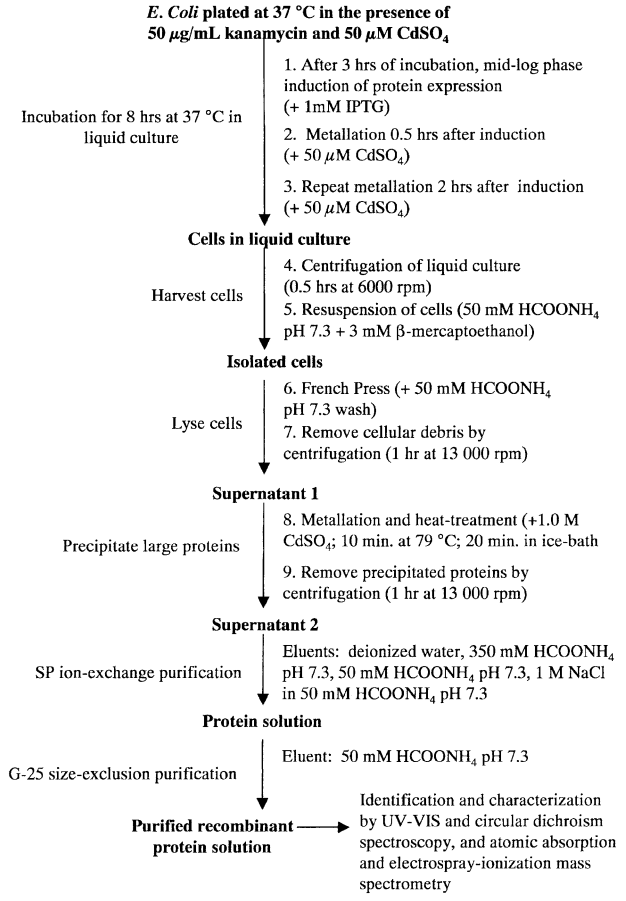


Fig. 5. Schematic representation of expression and purification procedure used to prepare the recombinant human metallothineins (reproduced with permission from Huang et al. [65]).

and the prospect of using molecular engineering to modify the sequence [65,66,69]. Recombinant proteins are made by inserting the gene (DNA) for MT into DNA vectors (plasmids) that can then be inserted into bacteria such as *Escherichia coli*. The bacteria are capable of expressing protein from both the plasmid DNA and its own DNA. Because of this, the protein can be mass-produced in much greater quantities and the production is of a single isoform of MT.

The steps involved in the preparation of protein that was used in our studies, Fig. 4, are shown in Fig. 5 [69]. This method was used to prepare the following protein sequences:

$M_4$-α-rhMT1+S-tag.
$M_3$-β-rhMT1+S-tag.
$M_7$-αβ-rhMT1+S-tag.
$M_7$-βα-rhMT1+S-tag (Fig. 4) [65].

Where M stands for the metal (either Cd or Zn) and rhMT1 stands for recombinant human MT1. The purpose of the S-tag is to stabilize the protein and prevent protein degradation.

## 3. Electrospray ionization mass spectrometry (ESI–MS)

The electrospray sample inlet uses an ionization method that promotes molecules and ions in solution into the gas phase as charged species. This technique works extremely well with a variety of ions dissolved in an array of solvents. The advantage of electrospray ionization mass spectrometry as a method for studying the metallated states of MT is that it is very sensitive and only small amounts of analyte are required. The revolutionary part of the technique is that we now have the capability of obtaining accurate masses of high molecular weight species such as proteins, nucleotides and polymers from dilute solutions [69–74].

There are three important distinguishing features of electrospray ionization mass spectrometry. (i) The atmospheric pressure ionization system generates a series of, multiply charged positive or negative ions. The ions may result from chemical or electrochemical processes. (ii) The analyte is introduced in a solution. This can allow for such hyphenated techniques as liquid chromatography mass spectrometry (LC–MS) and capillary electrophoresis mass spectrometry (CE–MS). These techniques are important methods for studying biological molecules. (iii) The electrospray ionization technique is quite 'soft', which means that instead of promoting fragmentation of the analyte molecule, the technique simply introduces positive or negative charges. This preserves, in many cases, the non-covalent interactions between molecules that exist in solution allowing the study of the three-dimensional aspects of the species. For our studies, this particularly applies to maintaining the structure of the metal binding domains inside the mass spectrometer [68,69].

The production of gas-phase ions has been described in terms of three steps. The first step is the generation and charging of the solution droplets that exit the capillary tip, second is the evaporation of solvent in the droplets, and the third is the production of gas-phase ions. In the experimental set up used to measure the pH dependence of the cadmium- and zinc-containing recombinant MTs shown in Fig. 6, a 10 μM solution of the protein in 5 mM formate buffer was eluted at a rate of 2–3 μl $min^{-1}$. The capillary potential was set to 4000 V. In Fig. 6, we also display the reconstruction of the parent molecule based on the charged states. This recalculation was carried out by the MD-SCIEX BIOTOOLS software, licensed to P.E. Sciex. The calculation matches all possible peaks to sequences of $(1+ \rightarrow n+)$ which are calculated to give the mass of the parent ion.

### 3.1. Recombinant human MTs with S tag in low and neutral pH

In Fig. 6A, we see a wide range of charge states for the α recombinant domain including a length of S-tag on the

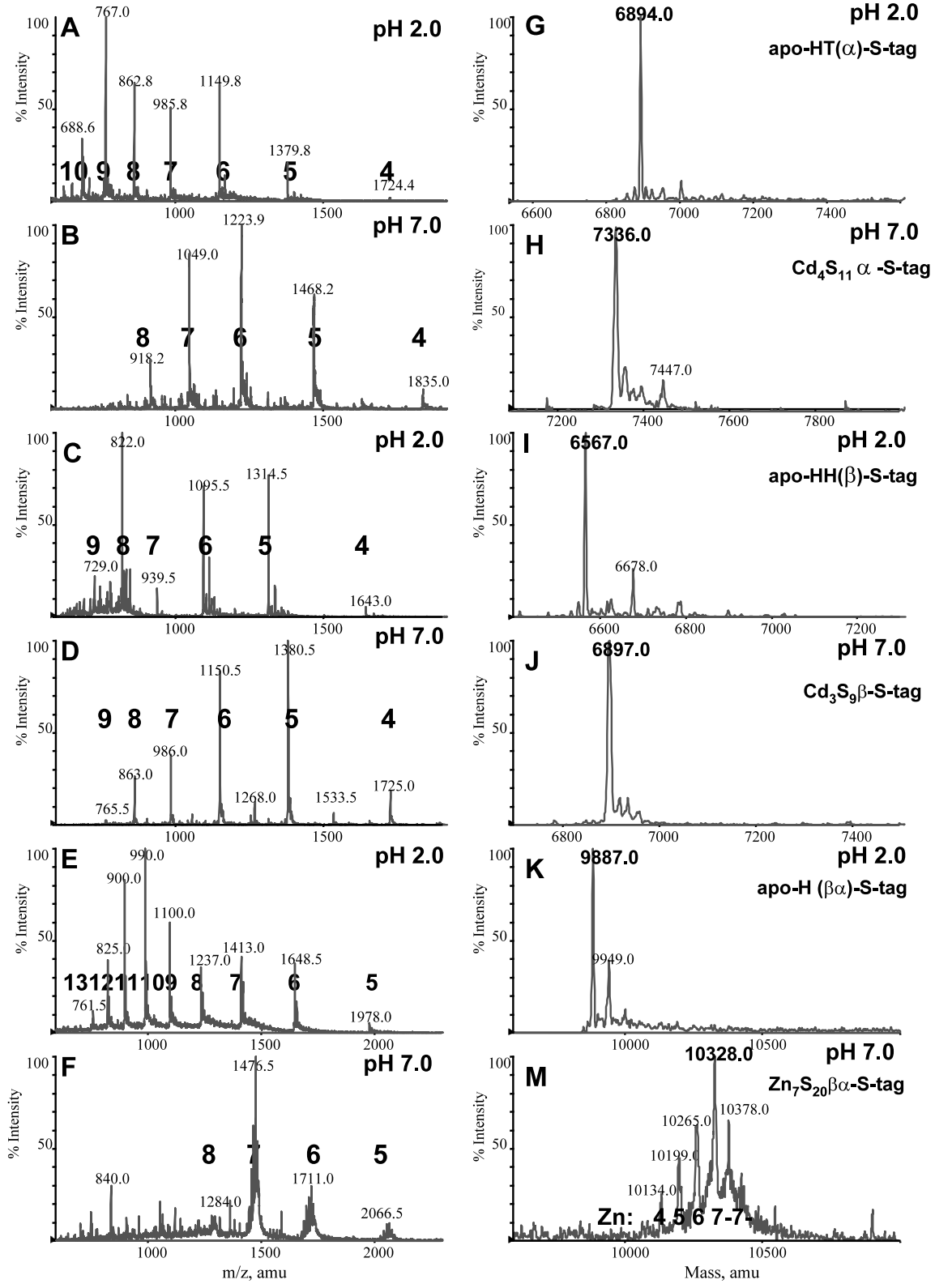


Fig. 6. ESI–MS data recorded for recombinant human MTs (with S-tag) at low and neutral pH, as charge states (left) and parent ion (right) [65]. The panels (A, B), (C, D) and (E, F) are the spectral data recorded for the protein when metal-free (pH 2) and metallated with cadmium (pH 7). The right hand side panels show the parent ions calculated using the charge states. A full description is in the text (reproduced with permission from Huang et al. [65]).

N-terminus (see Fig. 4 and Table 1) recorded at pH 2. These charge states which stretch from +10 to +4; all arise from the single metal free peptide species with a mass of 6894.0 amu as shown in Fig. 6G. The Figure (6B–F and H–M) shows the measured charge states and the calculated parents for three species of recombinant protein, measured under demetallated conditions (pH 2) and at neutral pH where the full complement of cadmium or zinc should be found. The mass of these proteins is higher than that found for native mammalian species because in these cases the peptide sequence of the S-tag has been incorporated into the structure (Table 1).

In Fig. 6A, we see the observed charge states for the α domain of MT at a pH of 2. There is a range of charge states from +10 to +4 observed. The presence of the two maxima, at 767 (+9) and 1149 (+6), suggest that there are two species in solution, in one the peptide is unfolded considerably more than in the other so that more sites are available for protonation. These two species have the same mass. In the reconstructed spectrum observed in Fig. 6G we can see the mass of 6894.0 amu which is the parent ion mass in the absence of metal. In the next spectrum, Fig. 6B, we see the observed charge states for the cadmium-containing α domain at neutral pH. Only a few predominant charge states are observed, the maximum at +6 is clearly an equilibrium between 5, 6, and 7. The mass of 7336.0 amu corresponds to the mass of the α domain bound to four cadmium atoms. This is expected because our native protein was induced with cadmium, and we do not expect the metals to be displaced at neutral pH. In Fig. 6C we see the observed charge states at pH of 2, for the β domain fragment. As with the α domain fragment, two maxima are found. The reconstruction (Fig. 6I) shows a majority species with a mass of 6567.0 amu. This mass corresponds to the metal free β domain. In Fig. 6D, the observed charge states for the β domain at pH of 7 can be reconstructed to give the cadmium bound domain with a mass of 6897.0 amu (Fig. 6J). This correlated to the β domain bound to three cadmium atoms. In Fig. 6E, we see the observed charge states for the two-domain, βα peptide at a pH of 2; with the increased chain length we find charge states extending from +13 to +5. Reconstruction (Fig. 6) gives a mass of 9887.0 amu, which corresponds to the metal free βα domain with S-tag containing 27 amino acids residues. Finally, Fig. 6F shows the charge states observed at pH of 7.0. Reconstruction shows a main mass peak of 10328.0 amu corresponding to the βα domain bound to seven zinc atoms.

The charge state data shown in Fig. 6A–F illustrate the effect of protein folding induced by metallation on the accessible, protonatable groups of the peptide chain. For example, in Fig. 6E, the unfolded peptide chain exhibits an equilibrium maximum in charge states of +10 and +11, whereas, when the zinc is bound the maximum charge state is +7. This effect is not just due to the pH, otherwise the surrounding +8 charge state would show increased intensity. We interpret this effect as being due to the folding of the peptide chain so that many protonatable sites are inaccessible. Much more detail is obtained when the protein is acidified in small steps, now, the demetallation and unfolding can be observed [69].

## 4. Kinetics of Cu(I) binding to metallothionein

Kinetic studies have been by far the most useful means used to interpret mechanisms by which chemical reactions proceed. Studies of chemical kinetics are concerned with the rates of chemical reactions and the factors upon which the rates depend, namely the effects of solvent, concentration, ionic strength, temperature and pH [41]. The use of chromophoric groups located in well defined regions of a protein have helped identify the steps involved in the folding or unfolding of each of these regions [75]. With respect to the metal binding reactions of MT, emission spectroscopy has been used to study the rate and specificity of copper (I) binding to the sulfurs of MT. These metal binding reactions were studied by monitoring the ligand-to-metal charge transfer emission band that results near 600 nm when the $Cu_n$–MT complex is excited with UV light at 290 nm [14,54,63].

The steady-state spectra shown in Fig. 7 [61,63,76] shows that emission at 600 nm increases as a function of copper loading. $Zn_7$–MT2A alone has no emission intensity in this region, but as successive Cu(I) ions are added to the protein the emission intensity at 600 nm becomes more apparent. The more Cu(I) ions bound to MT, the greater the emission intensity, however, this increase in emission intensity is far from linear, clearly showing the presence of two species [63]. Initially, a species forms that exhibits low intensity in the 600 nm region, after seven Cu(I) have been added, the intensity of the 600 nm band increases strongly on a per Cu(I)-added basis. For $Zn_7$–MT2A maximal emission intensity is observed for an addition of 12 Cu(I) ions per MT. EXAFS data suggests trigonal co-ordination geometry for Cu(I) to the sulfurs of rabbit liver MT with a final stoichiometry of $M_{12}S_{20}$ [40]; distributed as $M_6S_{11}$ for the α domain and $M_6S_9$ for the β domain. Therefore, the steady-state spectrum confirms that $Cu_{12}$–MT2A is the saturation point of MT. Additions past the saturation point, (additions >12 Cu(I) molar equivalents) decreased the emission intensity and a red shift in the $\lambda_{max}$ was also observed when compared with the $\lambda_{max}$ of the baseline and previous six copper additions.

The increase in emission intensity as 1–12 Cu(I) ions have been added to $Zn_7$–MT2A is a clear representation of how the ($Cu_6$–$S_{11}$)-α and ($Cu_6$–$S_9$)-β clusters formed

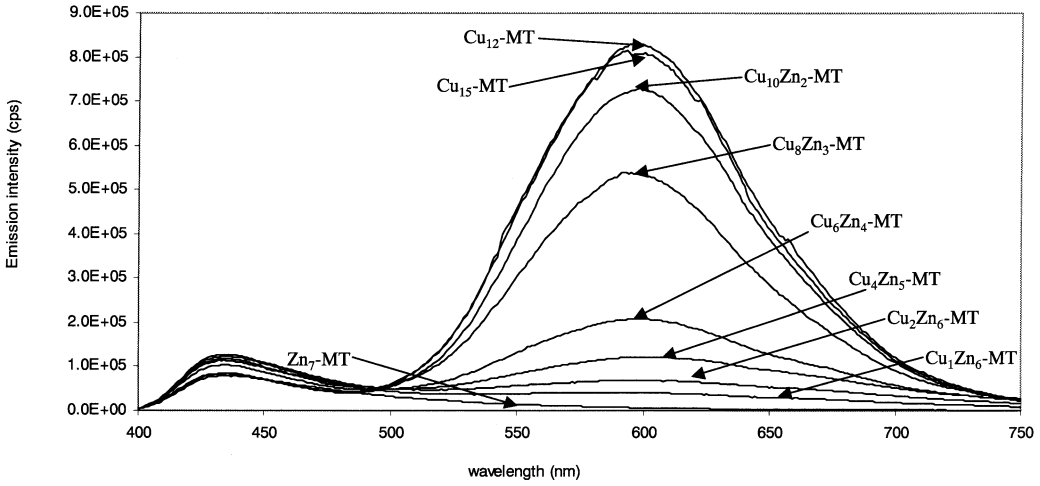


Fig. 7. Steady state emission spectra for each equimolar addition of Cu(I) to a 40 μM $Zn_7$MT2A protein solution at 20°C. Each spectrum was recorded at the end of each time-dependent measurements recorded for each copper(I) addition. Experimental methods: equimolar additions of Cu(I) from a solution of $[Cu(I)(CH_3CN)_4PF_6]$ dissolved in 30% (v/v) acetonitrile–water were added to an aqueous solution of 40 μM rabbit liver $Zn_7$–MT2A at 20°C; the change in emission intensity as Cu(I) ions bound to the cysteinyl sulfurs of MT and replaced the Zn(II) ions was monitored over time using a fluorolog-3 instrument ($\lambda_{ex} = 290$ nm and $\lambda_{em} = 600$ nm; reproduced with permission from Salgado et al. [76]).

become more efficiently shielded form the solvent. As two distinct metal–thiolate clusters are formed in the α and β domains of the protein due to the folding of the peptide backbone, the metal–thiolate cluster becomes protected from the solvent by the surrounding polypeptide chain. For $Zn_7$–MT2A, a maximum loading of 12 Cu(I) ions per MT molecule corresponds to a trigonal coordination geometry around each Cu(I) metal, so when $>12$ Cu ions are added to the protein up to a maximum of 15 Cu(I) per MT molecule, the emission intensity decreases and a red shift is observed. This characteristic drop in emission indicates that even though MT is able to bind up to 15 Cu(I), the peptide backbone had to unwind to try and accommodate these extra Cu(I) ions. As a result, solvent intrusion into the binding cage interfered with the LMCT; the solvent inactivated the $CuS_3$ clusters and decreased the emission intensity. The red shift observed for the $\lambda_{max}$ supports the idea that the trigonal coordination geometry of the Cu(I) ions in the binding cage was disrupted in order to form the $Cu_{15}$–MT2A species. A red shift has also been observed in the CD spectra recorded as Cu(I) is added to $Zn_7$–MT2A beyond the 12 Cu:MT stoichiometric ratio [61].

Time-dependent measurements are a measure of the change in emission intensity as a function of time. These data provide useful information about the structural (shape) changes that the polypeptide undergoes when binding and coordinating the incoming copper ions into the binding cage of the protein. As previously stated, tightly bound Cu(I) ions in the binding cage have a higher emission intensity than a more open structure which can no longer exclude the solvent from the $CuS_3$ units deactivating their excited state [63]. Fig. 8 [76] shows typical time-dependent emission data and the resultant calculated fitted line for the emission at 600 nm. The figure shows that as Cu(I) ions are added to the protein solution there is a rapid increase in emission intensity because it corresponds to the binding of the metal ions to the cysteinyl sulfurs of the protein (Cu(I)-

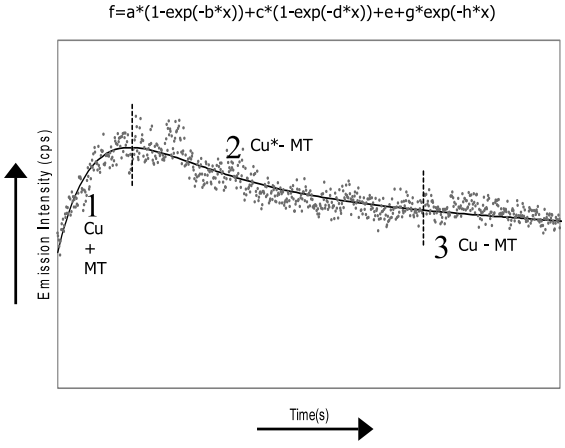


Fig. 8. Time-dependent measurements were collected for each equimolar addition of Cu(I) ions to $Zn_7$–MT2A until complete displacement of the Zn(II) ions has occurred and the fully metallated form of MT ($Cu_{12}$–MT2A) had been reached. Once final metallated product was obtained, the steady-state emission spectra of each Cu(I) addition was recorded between 400 and 750 nm with $\lambda_{ex} = 290$ nm. Sample of data analysis performed for the numerical analysis of all the time-dependent measurements collected. All curves were fitted to a triple exponential function of the form:

$$f = a(1 - \exp(-b \cdot x)) + c(1 - \exp(-d \cdot x)) + e + g\exp(-h \cdot x)$$

(equation parameters: $a = 11853$, $b = 0.2202$, $c = 6570.4$, $d = 0.0160$, $e = 6.0700E-06$, $g = 5495.0$, $h = 0.0016$) (reproduced with permission from Salgado et al. [76]).

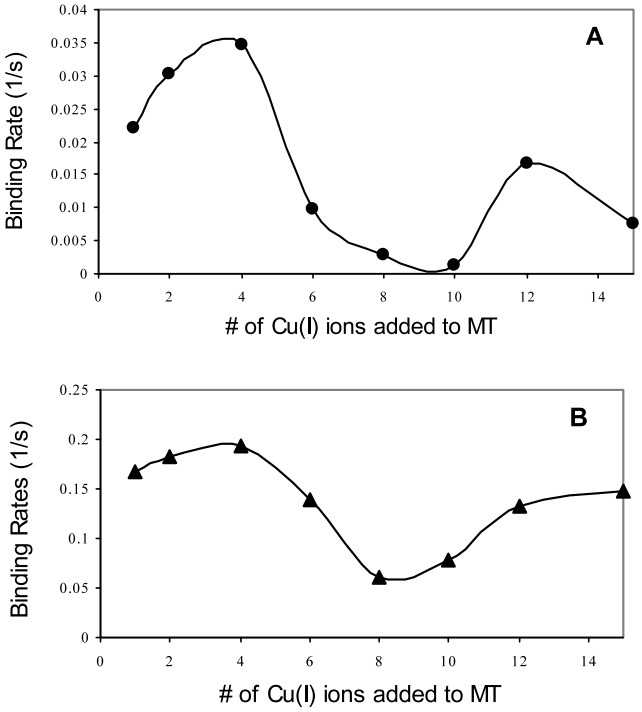


Fig. 9. The Cu(I) metal binding rates vs. the number of Cu(I) ions added to rabbit liver $Zn_7$–MT2A at two different temperatures, (A) 20 and (B) 38.5°C (rates were extracted from the data analysis of the time-dependent measurements shown in Fig. 8) (reproduced with permission from Salgado et al. [76]).

thiolates are luminescent even in aqueous solution). A brief plateau region and a rapid decrease in emission intensity then follow this increase. The observed drop in emission intensity with time during this third stage suggests that the metal ions are changing positions within the binding sites. The metal ions are rearranging in the binding sites until they find their most thermodynamically stable position and the polypeptide chain also folds into its most stable conformation.

Numerical analysis of the binding regions of the time-dependent measurements provide the binding rates for each Cu(I) ion that is added to MT. Fig. 9 [76] shows the binding rates calculated for Cu(I) additions (1–15) to solutions of 40 μM rabbit liver $Zn_7$–MT2A at 20 and 38.5 °C. The figure shows that the binding rates of successive Cu(I) ions number 1, 2 and 4, increase (become faster). Once the $Cu_4Zn_5$–MT2A complex has formed, further additions of Cu(I) decrease the binding rates thereby indicating that it becomes slower and slower to add copper ions to the MT system. The addition of the eighth Cu(I) ion appears to be a turning point in the metallation reaction of MT since the binding rates past eight Cu(I) take another turn and become faster, allowing the addition of the ninth to 12th Cu(I) ions to be easier. Finally, additions past 12 Cu(I), up to 15 Cu(I), slow down the binding rates of MT. Steady-State spectra have indicated that MT has a saturation point of 12 Cu(I) ions, which was characterized by maximal emission intensity near 600 nm.

We can interpret these results in terms of the metal coordination within the binding sites in the two domains. Initial binding of Cu(I) ions requires the displacement of $Zn^{2+}$ ions from the binding cage in order to achieve a trigonal coordination geometry. Because Cu(I) ions have a higher binding affinity for MT than Zn(II) ions, as more Cu(I) ions are added to MT, more zinc ions will be displaced. Once a $Zn^{2+}$ ion has been displaced, disruption of the metal–thiolate cluster has occurred and the binding of $Cu^{+}$ ions becomes faster. Past the addition of four Cu(I) ions, binding rates slow down because the number of possible positions where the Cu(I) ions can trigonally bind to MT decreases, and so bridging sulfur bonds must begin to form to stabilize the copper ions in the binding cage. Past the saturation point, the addition of three Cu(I) ions to the $Cu_{12}$–MT2A species becomes a slower process because it requires disruption of the metal–thiolate cluster already formed. When MT has reached its saturation point with copper(I) (maximum number of copper ions per sulfur atom), further unfolding of the polypeptide must take place to try and accommodate any extra copper ions, which in turn, would break up the $CuS_3$ stoichiometric units.

Metal binding reactions of MT are complex because a series of steps are required before the metal reaches a thermodynamically stable location in the binding cage. The dependency observed for the Cu(I) binding rates at different temperatures indicates that the structure in the region of the metal binding site is important. As the temperature is increased, the Cu(I) binding rates also increase, but a similar binding rate pattern is maintained for both temperatures as seen in Fig. 9A and B. Therefore, the folding mechanism of MT is a key factor in determining how fast metal ions will bind. The unique pattern observed for the binding rates of Cu(I) ions to MT provide an insight into the binding—rearrangement—equilibrium mechanism of other metal ions under similar conditions.

## 5. Scanning tunneling microscopy (STM)

In order to help determine the overall structures of protein molecules that cannot be determined by any other means, such as X-ray crystallography (when proteins do not crystallize) or NMR (when proteins aggregate at high concentrations or do not have NMR active isotopes), we currently employ the surface analysis technique scanning tunneling microscopy (STM). STM is a surface analysis technique that probes the electronic properties of surfaces and images the surface with atomic resolution [77]. A major benefit of this technique is that analysis is carried out without touching

the surface so that the sample remains intact. In order to understand the basic concept of STM operation, picture the operation of a record player; a pin is guided locally over the surface of a record which consists of a series of 'hills and valleys' of differing heights and depths. The variation in height, or topography, of the record's surface is output as sound. An STM instrument operates in much the same way. From STM, we can obtain size and shape information of protein molecules and correlate these results with molecular modeling techniques.

In our studies we use a Digital Instruments Nanoscope$^{TM}$ IIIa MultiMode SPM with a low-current STM head and NANOSCOPE III software is used. This STM instrument functions by applying a bias voltage between an atomically sharp, conducting probe (i.e. Pt–Ir tip) and a flat, conducting surface (i.e. highly oriented pyrolytic graphite (HOPG) or gold(111)) in close proximity ($<1$ nm). For a positively applied bias, electrons flow from the sample to the tip without the tip touching the sample. This electron flow is referred to as tunneling current. The tunneling current is exponentially dependent on the tip-sample surface separation [78] (a factor that makes this technique so sensitive) such that surface features differing in height result in changes in tunneling current. Within the image, variations in conductivity are output as variations in color contrast of a grayscale image, thereby appearing as a three-dimensional image (the brighter the pixels, the more conducting; the darker the pixels, the more insulating).

An STM instrument is capable of providing information about biological molecules adsorbed to the conducting surfaces. Biomolecules behave as insulators in an applied electric field such that in an STM image, one observes dark regions (non-conducting) in the locations where the biomolecules are present, surrounded by the light background areas of the conducting substrate. Some previously imaged biomolecules include DNA and RNA [79,80], enzymes such as catalase [81] and phosphorylase kinase [82], and various polypeptides including hemoglobin [83], cytochrome *c* [84] and cytochrome P450cam [85]. What separates this technique of biomolecule analysis from others such as NMR and EM is that it can provide atomic resolution (nanoscale images) of individual molecules, the samples can be imaged uncoated, and the sample is not affected by the imaging process. From these images the silhouette of the structures can be observed, and size and shape information can be obtained and compared with molecular modeling structures.

A study of rabbit MT using STM has been previously carried out by Davis and Hill [86]. Our current studies explore the structural information provided by STM imaging and correlate the findings with molecular models which take surface effects into account. The use of the STM instrument for studies of metalloproteins is still in the preliminary stages. At UWO, progress has been made in the molecular modeling aspect of this study. Fig. 10 is an energy minimized molecular model of rabbit liver $Zn_7$–MT on a gold surface, made using the CACHE molecular modeling software (version 5.0 MM2 and MD) [87]. For STM studies we use gold substrates in order to take advantage of the Au–S bonding from the sulfurs of the metal–thiolate clusters to the gold surface. Alkanethiols, commonly used in the formation of self-assembled monolayers (SAMs), adsorb to gold surfaces through their sulfur functionality and have been shown to stand vertically on the surfaces of gold [88]. One may expect a similar structural orientation from MT adsorbed to a gold surface through the exposed sulfur groups of the metal–thiolate clusters. Computational methods such as MD can be used to model the conformations of molecules based on energy minima. The typical MD calculations carried out by Stillman et al. normally employ high temperatures in order to search for global minima by relaxing strained bonds. When modeling the adsorption of molecules on a surface, MD calculations also provide information about steric interactions imposed by the surface.

Models of MT docked on a gold surface were constructed in order to determine the effect of a gold substrate on the structure of the protein. MD–MM2 cycles were carried out at 1000 K for 300 ps on a molecular model of recombinant human $Cd_7$–MT with no S-tag, docked on a single-layer Au(111) surface by a terminal sulfur of the β domain of the MT through a single weak bond (Fig. 10) [87] using CACHE molecular modeling software version 5.0. This model was constructed based on previous calculations carried out by Stillman and Fowle [27], as well as calculations described in the following section [28,100]. The molecule of protein appears to lie horizontally across the surface contrary to the orientation observed in SAMs. The exposed metal–thiolate clusters of each domain appear to face opposite directions, suggesting the coordinated metals of the α domain are accessible for imaging by STM, and the methionine of the α domain appears to have docked itself onto the surface, thereby increasing the restriction of movement on the surface. The dumbbell shape of the protein appears to remain intact on the surface.

A series of molecular modeling experiments were carried out on this model at increased temperatures (ranging from 1000 to 1600 K) and varying lengths of time in order to study the motion of the two domains on the surface with respect to each other. Given that the α domain is not ligated to the surface, one may expect it to move away from the surface, given enough thermal energy. According to the results of these calculations, there is little variation in the structure between high temperature models (not shown) and the low temperature model shown in Fig. 10. Molecular modeling calculations carried out on the protein itself resulted in

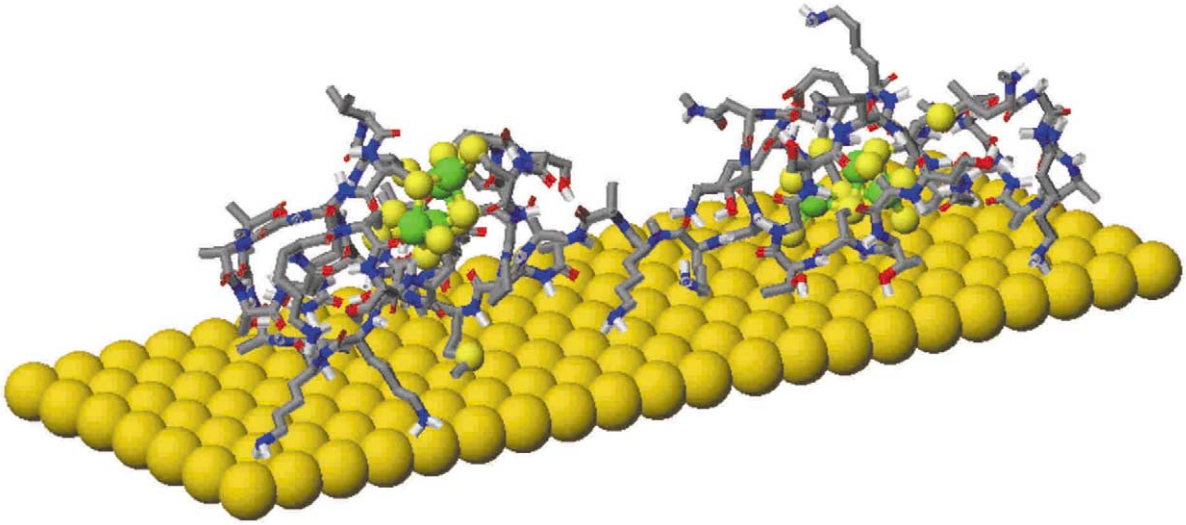

Fig. 10. Energy minimized structure of recombinant human $Cd_7$–MT2A bound to a Au(III) surface by one weak bond through an exposed terminal sulfur of the β domain. Minimization was carried out by a combination of molecular mechanics (MM2) and MD (100 K; 100 ps). The primary structure is shown with bonds for the peptide and van der Waals radii for the metal–thiolate clusters. One layer of Au(111) is shown. Atom legend: green = Cd(II), light yellow = S, gray = C, blue = N, red = O, dark yellow = Au(III) (reproduced with permission from Chan et al. [87]).

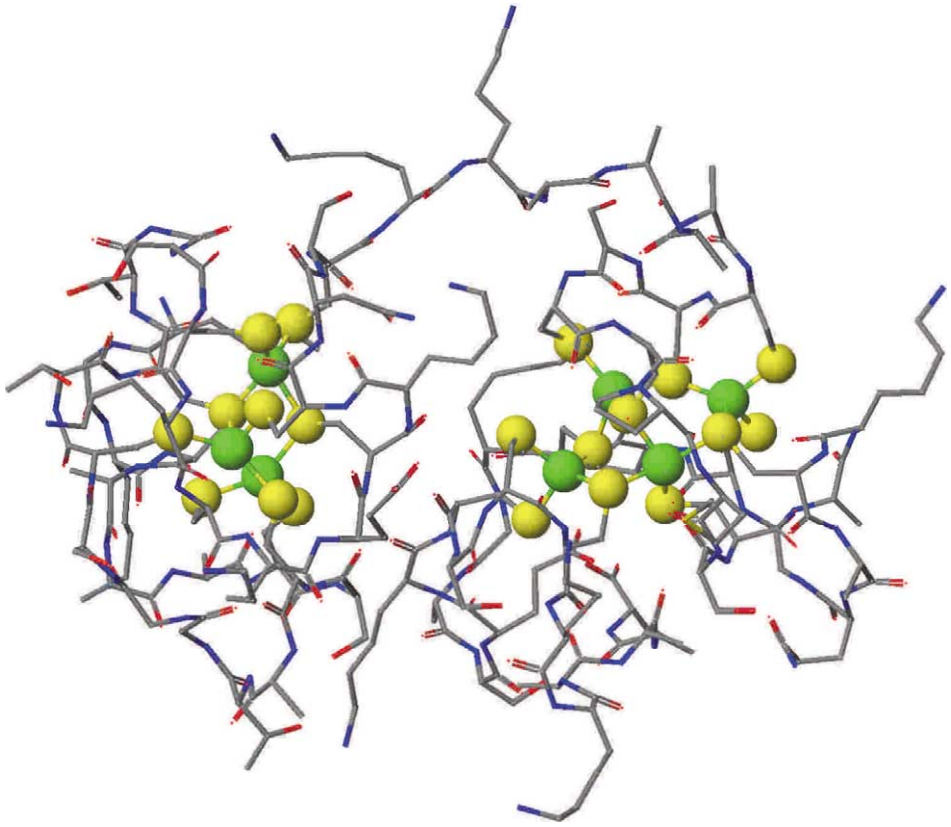

Fig. 11. Energy minimized structure of recombinant human $Cd_7$–MT2A. The primary structure is shown with bonds for the peptide and van der Waals radii for the metal–thiolate clusters. The molecular mechanics (MM2) and MD calculations were used in combination. MD was carried out for 100 ps at 1000 K. Atom legend: green = Cd(II), light yellow = S, gray = C, blue = N, red = O (reproduced with permission from Chan et al. [87]).

the domains swinging together, forming a tight, compact structure (Fig. 11) [87]. In comparison to the results of the protein adsorbed to the gold surface, the models suggest that the gold surface restricts the movement of the two domains. STM analysis of such a sample will be carried out to determine the validity of these models.

## 6. Molecular modeling

The structure and metal–cysteine connectivities for mammalian MT ($M_7^{II}$–MT) have been previously elucidated in detail by analysis of a combination of $^1$H-NMR and 2D $^{113}$Cd-NMR data [89,90] for a number of different Cd(II) and Zn(II) containing proteins [89–92] and by X-ray crystallography for rat liver $Cd_5Zn_2$–MT [35,36]. The C-terminal α domain contains 11 cysteine residues and binds four M(II) ions, while the N-terminal β domain binds three M(II) ions with nine cysteinyl residues, Figs. 1 and 2. The connectivities, which were determined for Cd–$S_{cys}$ and later for Zn–$S_{cys}$ using a combination of $^{113}$Cd and $^1$H-NMR experiments, are shown in Figs. 1 and 4, specifically for the 62-amino acid rabbit liver isoform two protein. Metal replacement studies have shown that the seven Zn(II) ions found in $Zn_7$–MT can be replaced by metals of greater binding strength such as Cd(II). Optical studies of these metal ion titration experiments suggest that Cd(II) replaces Zn(II) isomorphously with the retention of specific Zn–$S_{cys}$ connectivities and the overall structure of the binding site [14,43,45,51]. $^1$H-NMR data also confirm that the overall structures of the cadmium- and zinc-containing mammalian proteins are the same [32,33]. EXAFS studies have provided bond lengths and coordination numbers for $Zn_7$–MT, $Cu_{12}$MT, $Ag_{12}$MT, $Hg_{17}$MT, $Hg_{18}$MT, and $Cd_7$–MT [14,37–40]. Interestingly, while the EXAFS data for the $Zn_7$MT2A could be analyzed with extremely low standard errors, indicating a very similar set of bond lengths and coordination numbers, the data for the $Cd_7$–MT2A protein showed much greater variation, indicating perhaps that there was more variability in the bond lengths and angles for the seven Cd(II) atoms [37–40]. The molecular modeling also suggests this [27]. Reports describing modeling of the 3D structure of a number of different MTs have recently been published [27,93,94].

The determination of these structures greatly aids studies of many properties of the protein. For example, the mechanism for metallation is largely unknown, calculations can suggest routes that are energetically favorable. In our work with the STM, we have used the calculated protein docked on to the gold surface to show the overall silhouette expected. The objective of this work was to develop molecular models specifically for the mammalian protein and its fragments using molecular mechanics calculations based on known connectivities and force field parameters modified for each metal. We describe here structures calculated using molecular modeling techniques for the $Zn_7$–MT and $Cd_7$–MT rabbit liver proteins. The 3D structural dynamics behavior was investigated with a MD simulation at a number of temperatures. Questions concerning the effect of increased linker length between the α and β domain fragments can be answered from the MD results.

### 6.1. Computational details and construction of the model

The modeled structure for the $Zn_7$–MT2A species was constructed using three constraints: the primary amino acid sequences shown in Fig. 1, the Cd–$S_{cys}$ connectivity data [31,32,89,94,95], and the protein wrapping found in the rat liver $Cd_5Zn_2$–MT crystal structure [35,36]. All calculations were performed using the CACHE three-dimensional Stereo Worksystem [96] using Allinger's MM2 force field [97] as augmented by CACHE. The molecular mechanics structure was investigated by comparing the total energy of possible structures, where the energy is given by the mechanics equation as follow:

$$E_{\text{total}} = E_{\text{bonding}} + E_{\text{theta}} + E_{\text{phi}} + E_{\text{improp}} + E_{\text{elec}} + E_{\text{vdw}} + E_{\text{H bond}}$$

where these terms describe the energies involved in the bond, angles, dihedral angles, improper torsions, electrostatic potential, van der Waals interactions, and hydrogen bonding, respectively. The CACHE system uses the parameters published by Allinger [97] for the MM2 force field directly for all elements except for the metals. There are no force field parameters available for metals, rather the CACHE system provides proprietary estimates of the force field parameters for each element in the Periodic Table. The key parameters of bond stretching and bond bending for each metal–thiolate bond (Zn–S and Cd–S) were modified from our previous studies: (i) bond stretch, $E = 143.88k_s[(r-r_0)^2-(r-r_0)^3]/2$, where $k_s = 4.400$ mdyn Å$^{-1}$ (bond stiffness) and standard length $r_0 = 2.374$ Å (for $Zn^{II}$ with bridging S), 2.286 Å (for $Zn^{II}$ with terminal S), based on the X-ray diffraction data of model compounds reported by Hencher et al. [98], and 2.560 Å (for $Cd^{II}$ with bridging S) and 2.467 Å (for $Cd^{II}$ with terminal S) based on the X-ray diffraction data of model compounds reported by K.S. Hagen and R.H. Holm [99] for tetrahedral coordination; and (ii) bond angle, $E = 0.043828k_b[(\theta-\theta_0)^2+7.0\times10^{-8}(\theta-\theta_0)^6]/2$, where $k_b = 0.450$ mdyn Å$^{-1}$ (bond stiffness) and $\theta = 109.470^\circ$ (the standard angle for tetrahedral coordination) and 94.300° (the standard angle of metal–thiolate–metal). These parameters provide a starting structure

that explicitly lengthens the bridging metal–thiolate bond lengths.

MD simulations approximate the real motion of a molecular system in a vacuum by using the same force field equations that describe the potential energy of the molecular geometries to evaluate the forces on each atom. The kinetic energy of a molecular system is derived from the atomic velocities, which in turn are chosen to reflect the temperature of the simulation. By integrating Newton's equation of motion, atomic velocities can be obtained from the force on each atom. For a given temperature, an initial set of velocities can be selected from the Maxwell–Boltzmann distribution and a trajectory through time can be generated for any molecular system. This dynamics simulation conserves the total (potential plus kinetic) energy, and the volume of the entire system. This type of simulation is also known as a microcanonical ensemble at a defined temperature. In the CACHE dynamics simulation, the molecule remains centered with no rotation, that is, with no net translational or rotational momenta. The motion observed are only vibrational (stretching, bending, and internal rotation) motions of the atoms where their average velocities are determined from the relationship among their average velocities and temperature as well as their mass.

The model of the MT peptide was constructed as follows. Initially, metal free models of the α and β domains were created by docking the amino acid residues using the CACHE Editor application. The CACHE Editor application and the three-dimensional stereo display were then used to adjust the positions of the residues and side chains to mimic the wrapping and folding of the rat liver $Cd_5Zn_2$–MT crystal structure and the structures for rabbit liver MT determined by NMR [35,36]. Seven Zn(II) ions with $sp^3$ hybridization were inserted into the protein structure and then bound to the corresponding thiolate groups possessing a unit negative charge and $sp^3$ hybridization. Force field parameters were defined for terminal or bridging sulfurs. The conjugate gradient method was utilized in the minimization of the structure, using the augmented MM2 parameters modified as above and treating the methylene and methyl groups explicitly. The molecular geometry was then optimized by the molecular mechanics MM2 tool in CACHE 4.5 in the gas phase at 0 K and refined until the energy change was less than 0.001 kJ $mol^{-1}$. The $Cd_7$–MT2A model was created by replacing the seven Zn(II) ions with Cd(II) ions possessing the same charge and geometry, and re-minimizing the structure using the MM2 parameters modified as mentioned above. This mimics the isomorphous replacement of Zn(II) by a metal that adopts the same coordination geometry [43,56].

Like all mathematical modeling, the first guess of the metalloproteins' structure involves a number of critical assumptions including the connectivities between each atom, and the coordination group as well as the sequence of amino acids. For metals this means that the coordination number and hybridization must be known or assumed so that the correct geometry can be set for their calculation. For Cd(II) and Zn(II) in MT, tetrahedral coordination requires four cysteinyl groups. The minimization can only show how the peptide will wrap under these constraints, not whether a different coordination number would give a lower total energy. By examining the structure in detail one can determine if it is reasonable.

In order to explore the conformational behavior of rabbit liver $Zn_7$–MT2A and $Cd_7$MT2A, we performed MD simulations (MM2–MD) on each of these structures from 0 K to a given temperature using the same force field parameters as the molecular mechanics, Fig. 2.

### 6.2. Molecular mechanics

#### 6.2.1. The $Cd_7$–MT2A structure

Fig. 12 [100] shows the space-filling and tube representations of this minimized structure for rabbit liver

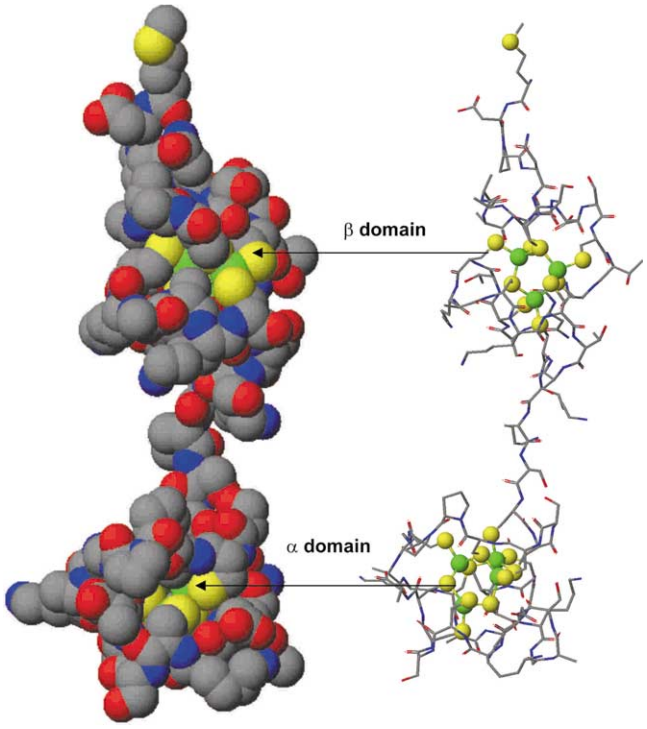


Fig. 12. Space-filling (left) and tube, ball and stick (right) representation of the rabbit liver $Cd_7$–MT2A or $Zn_7$–MT2A model calculated by molecular mechanics (MM2). The peptide wrapping around the binding cluster is displayed in a tube representation. The Zn(II) or Cd(II)-thiolate clusters appear to be embedded within the peptide chain, however, crevices are seen in the space-filling representation may provide solvent and metal ions access to the binding clusters. Atom legend: green = Zn(II) or Cd(II), yellow = S, gray = C, blue = N, red = O (reproduced with permission from Huang et al. [65]).

Table 2
Connectivities and lengths of Cd(II)-thiolate in the rabbit liver MT2A structure from MM2 calculations (data from ref. [100])

| β Domain | | | α Domain | | |
|---|---|---|---|---|---|
| Cd–$S_{cys}$ connectivity | Bridging/terminal $S_{cys}$ | Cd–S bond length (pm) | Cd–$S_{cys}$ connectivity | Bridging/terminal $S_{cys}$ | Cd–S bond length (pm) |
| Cd1–S5 | Terminal | 246.8 | Cd4–S51 | Bridging | 254.4 |
| Cd1–S7 | Bridging | 256.4 | Cd4–S58 | Terminal | 247.5 |
| Cd1–S22 | Terminal | 247.7 | Cd4–S60 | Terminal | 248.2 |
| Cd1–S25 | Bridging | 257.5 | Cd4–S61 | Bridging | 257.1 |
| Cd2–S7 | Bridging | 256.4 | Cd5–S35 | Bridging | 257.3 |
| Cd2–S14 | Terminal | 246.7 | Cd5–S37 | Terminal | 248.4 |
| Cd2–S16 | Bridging | 256.5 | Cd5–S38 | Bridging | 255.6 |
| Cd2–S27 | Terminal | 246.9 | Cd5–S51 | Bridging | 255.9 |
| Cd3–S16 | Bridging | 255.9 | Cd6–S34 | Terminal | 247.4 |
| Cd3–S20 | Terminal | 245.8 | Cd6–S35 | Bridging | 259.6 |
| Cd3–S25 | Bridging | 256.2 | Cd6–S45 | Bridging | 261.7 |
| Cd3–S30 | Terminal | 247.6 | Cd6–S49 | Terminal | 250.0 |
| | | | Cd7–S38 | Bridging | 254.0 |
| | | | Cd7–S42 | Terminal | 246.9 |
| | | | Cd7–S45 | Bridging | 256.8 |
| | | | Cd7–S61 | Bridging | 257.6 |
| | | Mean Cd–S bond lengths: 251.7±5.1 | | | Mean Cd–S bond lengths: 253.7±4.9 |

Mean of terminal Cd–S bond lengths: 247.5±1.1 pm.
Mean of bridging Cd–S bond lengths: 256.8±1.9 pm.
Total mean Cd–S bond lengths: 252.8±4.9 pm.

$Cd_7$–MT2A. The bond lengths, bond angles and selected interatomic distances are listed in Tables 2–4, respectively. These figures show that the structure is essentially the same as $Zn_7$–MT2A described below. There are, however, a couple of differences between these structures. Firstly, the Cd(II) thiolate binding cluster is noticeably elongated compared with its Zn(II)-thiolate counterpart, although the overall shape of the binding cluster remain constant, and secondly, the crevices located in the α and β domains appear to be considerably larger, as seen in Fig. 12.

### 6.2.2. The $Zn_7$–MT2A structure

The calculated rabbit liver $Zn_7$–MT2A structure shown in Fig. 12 [100] was carried out using the amino acid sequence of rabbit liver MT2A. We have titrated rabbit liver $Zn_7$–MT with Cd(II), Cu(I), Hg(II), Ag(I) and Au(I), monitoring the metal exchange and subsequent rearrangement reactions spectroscopically [14,27,46–49,61]. The circular dichroism spectrum, in particular, can provide strong evidence for changes in the overall structure of the binding site and whether the peptide chain alters its path as each Zn(II) is exchanged. The significance of this type of spectra is that the CD spectrum arises from the chirality of the entire binding site rather than from the chirality of individual $MS_4$ group, thus when Zn(II) is replaced by a new metal with high atomic number such as Cd(II), a red-shift in the band center is observed indicating that the S-to-M charge transfer band shifts to longer wavelengths. If the overall wrapping of the peptide chain around the new metals is the same as that of the Zn(II), then we do

Table 3
Interatomic distances (pm) of the nearest cadmium atoms in the Cd(II)-thiolate for each domain in the rabbit liver $Cd_7$–MT2A structure minimized by MM2

| β Domain | | α Domain | |
|---|---|---|---|
| Nearest Cd–Cd atom | Cd–Cd distance (pm) | Nearest Cd–Cd atom | Cd–Cd distance (pm) |
| Cd(1)–Cd(2) | 406.8 | Cd(4)–Cd(5) | 401.1 |
| Cd(2)–Cd(3) | 393.6 | Cd(4)–Cd(7) | 430.7 |
| Cd(1)–Cd(3) | 402.0 | Cd(5)–Cd(6) | 402.9 |
| | | Cd(5)–Cd(7) | 397.5 |
| | | Cd(6)–Cd(7) | 400.8 |
| Mean | 400.8 | Mean | 406.6 |

Mean Cd–Cd distance in β and α domains: 404.4 pm.

Table 4
Connectivities and bond angles for domains of rabbit liver MT2A from MM2 calculation (data from [100])

| β Domain | | | | α Domain | | | |
|---|---|---|---|---|---|---|---|
| S–Cd–S | | Cd–S–Cd | | S–Cd–S | | Cd–S–Cd | |
| Connectivity | Bond angle (°) | Connectivity | Bond angle (°) | Connectivity | Bond angle (°) | Connectivity | Bond angle (°) |
| $S_7$–$Cd_1$–$S_5$ | 92.4 | $Cd_3$–$S_{25}$–$Cd_1$ | 103.0 | $S_{61}$–$Cd_4$–$S_{60}$ | 129.4 | $Cd_4$–$S_{61}$–$Cd_7$ | 113.6 |
| $S_{22}$–$Cd_1$–$S_5$ | 99.3 | $Cd_3$–$S_{16}$–$Cd_2$ | 100.4 | $S_{61}$–$Cd_4$–$S_{58}$ | 103.6 | $Cd_5$–$S_{51}$–$Cd_4$ | 103.6 |
| $S_{22}$–$Cd_1$–$S_7$ | 118.3 | $Cd_2$–$S_7$–$Cd_1$ | 105.0 | $S_{61}$–$Cd_4$–$S_{51}$ | 116.9 | $Cd_5$–$S_{35}$–$Cd_6$ | 102.4 |
| $S_{22}$–$Cd_1$–$S_{25}$ | 108.2 | | | $S_{60}$–$Cd_4$–$S_{58}$ | 115.2 | $Cd_5$–$S_{38}$–$Cd_7$ | 102.5 |
| $S_{25}$–$Cd_1$–$S_7$ | 111.5 | | | $S_{60}$–$Cd_4$–$S_{51}$ | 89.8 | $Cd_6$–$S_{45}$–$Cd_7$ | 101.3 |
| $S_{25}$–$Cd_1$–$S_5$ | 127.2 | | | $S_{58}$–$Cd_4$–$S_{51}$ | 97.4 | | |
| $S_7$–$Cd_2$–$S_{14}$ | 105.5 | | | $S_{35}$–$Cd_5$–$S_{37}$ | 131.2 | | |
| $S_7$–$Cd_2$–$S_{16}$ | 101.8 | | | $S_{35}$–$Cd_5$–$S_{51}$ | 101.0 | | |
| $S_7$–$Cd_2$–$S_{27}$ | 113.0 | | | $S_{35}$–$Cd_5$–$S_{38}$ | 98.4 | | |
| $S_{14}$–$Cd_2$–$S_{16}$ | 104.2 | | | $S_{37}$–$Cd_5$–$S_{51}$ | 98.7 | | |
| $S_{14}$–$Cd_2$–$S_{27}$ | 110.4 | | | $S_{37}$–$Cd_5$–$S_{38}$ | 103.6 | | |
| $S_{16}$–$Cd_2$–$S_{27}$ | 120.7 | | | $S_{51}$–$Cd_5$–$S_{38}$ | 128.1 | | |
| $S_{16}$–$Cd_3$–$S_{20}$ | 109.6 | | | $S_{49}$–$Cd_6$–$S_{45}$ | 116.2 | | |
| $S_{16}$–$Cd_3$–$S_{25}$ | 109.6 | | | $S_{49}$–$Cd_6$–$S_{35}$ | 109.6 | | |
| $S_{16}$–$Cd_3$–$S_{30}$ | 114.5 | | | $S_{49}$–$Cd_6$–$S_{34}$ | 100.5 | | |
| $S_{20}$–$Cd_3$–$S_{25}$ | 94.8 | | | $S_{45}$–$Cd_6$–$S_{35}$ | 124.1 | | |
| $S_{20}$–$Cd_3$–$S_{30}$ | 103.0 | | | $S_{45}$–$Cd_6$–$S_{34}$ | 93.1 | | |
| $S_{25}$–$Cd_3$–$S_{30}$ | 122.5 | | | $S_{35}$–$Cd_6$–$S_{34}$ | 108.7 | | |
| | | | | $S_{38}$–$Cd_7$–$S_{42}$ | 99.2 | | |
| | | | | $S_{38}$–$Cd_7$–$S_{45}$ | 106.9 | | |
| | | | | $S_{38}$–$Cd_7$–$S_{61}$ | 106.3 | | |
| | | | | $S_{42}$–$Cd_7$–$S_{45}$ | 105.0 | | |
| | | | | $S_{42}$–$Cd_7$–$S_{61}$ | 110.6 | | |
| | | | | $S_{45}$–$Cd_7$–$S_{61}$ | 125.7 | | |
| Mean values | 109 ± 9.94 | Mean values | 102.8 ± 2.3 | Mean values | 109.1 ± 11.9 | Mean values | 104.7 ± 5.1 |

Total mean value of S–Cd–S: 109.2 ± 10.7.
Total mean value of Cd–S–Cd: 104.0 ± 4.1.

not anticipate there being any change in the CD spectral envelope in the region of this charge transfer band. However, if there is a change in connectivity such that different sulfurs are connected to the new metal in the old location, or if the protein folds in a different manner around the M-Cys region, the CD spectral envelope will change in sign and magnitude. The CD data measured as Cd(II) displaced Zn(II) have been interpreted as indicating a complete retention of the structural features of $Zn_7$–MT2A. Moreover, similar conclusions have been reached from $^1$H-NMR studies of human Zn–MT and Cd–MT [95]. These reported results allows us to model the structure of rabbit liver $Zn_7$–MT2A using the same connectivities as for the Cd(II) parent. Fig. 12 shows the results of the calculation for the structure of $Zn_7$–MT2A from rabbit liver. The two metal–thiolate binding clusters $Zn_3S_9$ (β) and $Zn_4S_{11}$ (α) are clearly located within binding sites defined by the wrapping of the peptide chain. These clusters are nearly identical to the corresponding clusters found in the X-ray structure [35,36].

Selected interatomic distances and angles are compiled in Tables 5–7. The mean Zn–S bond lengths of 234.9 pm (see Table 5) determined by the molecular mechanics calculation is identical to the bond length reported by previous XAFS studies [37–40]. The mean $Zn–S_{term}$ bond length is 8.9 pm smaller than that of $Zn–S_{brid}$ bonds, where $Zn–S_{term}$ indicates a bond to a terminal sulfur and $Zn–S_{brid}$ indicates a bond to a bridging sulfur. These values span the mean Zn–S distance (234.9 pm) in tetrahedral $Zn_7(Cys–S)_{20}$. The mean $Zn–S_{term}$ distance is at the higher end of the range (236.8–240.6 pm) similar to the distances in tetrahedral $Zn_7(Cys–S)_{20}$. The overall wrapping of the peptide chain in the structure calculated for $Zn_7$–MT2A shown in Fig. 12, is in good agreement with the folding shown in the X-ray crystallographic representation of rat liver $Cd_5Zn_2$–MT [35,36]. The space-filling representation can be used in conjunction with the tube representation to determine which amino acids are located on the surface.

### 6.3. Molecular dynamics simulation

To explore the conformational behavior of the molecule, a MD (MM2–MD) simulation was applied to rabbit liver $Zn_7$–MT2A at different defined temperatures. The common starting geometry was obtained

Table 5
Connectivities and lengths of Zn(II)-thiolate in the rabbit liver MT2A structure from MM2 calculations (data from [100])

| β Domain | | | α Domain | | |
|---|---|---|---|---|---|
| Zn–$S_{cys}$ connectivity | Bridging/ terminal $S_{cys}$ | Zn–S bond length (pm) | Zn–$S_{cys}$ connectivity | Bridging/ terminal $S_{cys}$ | Zn–S bond length (pm) |
| Zn1–S5 | Terminal | 229.4 | Zn4–S51 | Bridging | 236.4 |
| Zn1–S7 | Bridging | 238.5 | Zn4–S58 | Terminal | 229.7 |
| Zn1–S22 | Terminal | 230.2 | Zn4–S60 | Terminal | 230.5 |
| Zn1–S25 | Bridging | 239.5 | Zn4–S61 | Bridging | 239.3 |
| Zn2–S7 | Bridging | 238.3 | Zn5–S35 | Bridging | 239.4 |
| Zn2–S14 | Terminal | 229.0 | Zn5–S37 | Terminal | 230.6 |
| Zn2–S16 | Bridging | 238.2 | Zn5–S38 | Bridging | 237.1 |
| Zn2–S27 | Terminal | 229.0 | Zn5–S51 | Bridging | 237.9 |
| Zn3–S16 | Bridging | 237.6 | Zn6–S34 | Terminal | 229.8 |
| Zn3–S20 | Terminal | 228.1 | Zn6–S35 | Bridging | 241.5 |
| Zn3–S25 | Bridging | 238.2 | Zn6–S45 | Bridging | 243.7 |
| Zn3–S30 | Terminal | 230.1 | Zn6–S49 | Terminal | 232.2 |
| | | | Zn7–S38 | Bridging | 235.6 |
| | | | Zn7–S42 | Terminal | 229.1 |
| | | | Zn7–S45 | Bridging | 238.9 |
| | | | Zn7–S61 | Bridging | 239.6 |
| | | Mean Zn–S bond lengths: $233.8 \pm 4.8$ | | | Mean Zn–S bond lengths: $235.7 \pm 4.7$ |

Mean of terminal Zn–S bond lengths: $229.8 \pm 1.0$ pm.
Mean of bridging Zn–S bond lengths: $238.7 \pm 1.9$ pm.
Total mean Zn–S bond lengths: $234.9 \pm 4.8$ pm.

from the MM2 structures described above. The evolution of energy and temperature for MD trajectories of the rabbit liver $Zn_7$–MT2A and $Cd_7$–MT2A were carried out within a specified time period at increasing temperatures. Interesting dynamic phenomena were observed at elevated temperatures in the MD trajectories during the simulation. MD snapshots of the 3D structural conformers of rabbit liver $Zn_7$–MT2A as a function of time at 300 K are depicted in Fig. 13 [100]. From an analysis of the MD trajectory data, it is apparent that the two domains (α and β) were restricted by the tetrahedral coordination of the model and the positions of cysteinyl residues were very stable over the course of the dynamics simulation. Conversely, the N- and C-termini, as well as the linker residues, exhibited greater conformational flexibility and fluctuation, as they were relatively unrestrained by the bound metals. Charged amino acid acids such as lysine and aspartic acid located, respectively, on the linker and the N-terminus, interacted with other amino acids to form the folded structures. During this stage of the calculations, tightly folded conformers with low total energy were formed at about 20 ps at 300 K.

Fig. 14 [100] shows the 3D structural conformers of rabbit liver $Cd_7$–MT2A as a function of time at 300 K in MD trajectory snapshots. The folding process of the protein was observed as for the rabbit liver $Zn_7$–MT2A mentioned above. One of the lysines in the linker shifted towards an amino acid with negatively charged groups in β domain, and another lysine shifted towards a charged negative amino acid in the α domain as a result of H-bonding and hydrophobic interactions. The two

Table 6
Interatomic distances (pm) of the nearest zinc atoms in the Zn(II)-thiolate for each domain in the rabbit liver $Zn_7$–MT2A structure minimized by MM2

| β Domain | | α Domain | |
|---|---|---|---|
| Nearest Zn–Zn atom | Zn–Zn distance (pm) | Nearest Zn–Zn atom | Zn–Zn distance (pm) |
| Zn(1)–Zn(2) | 384.1 | Zn(4)–Zn(7) | 404.5 |
| Zn(2)–Zn(3) | 370.1 | Zn(5)–Zn(6) | 379.9 |
| Zn(1)–Zn(3) | 385.2 | Zn(5)–Zn(7) | 370.4 |
| | | Zn(6)–Zn(7) | 375.9 |
| | | Zn(4)–Zn(5) | 377.8 |
| Mean | 379.8 | Mean | 381.7 |

Mean Zn–Zn distance in β and α domains: 381.0 pm.

Table 7
Connectivities and bond angles for domains of rabbit liver MT2A from MM2 (data from [100])

| β Domain | | | | α Domain | | | |
|---|---|---|---|---|---|---|---|
| S–Zn–S | | Zn–S–Zn | | S–Zn–S | | Zn–S–Zn | |
| Connectivity | Bond angle (°) | Connectivity | Bond angle (°) | Connectivity | Bond angle (°) | Connectivity | Bond angle (°) |
| $S_7$–$Zn_1$–$S_5$ | 92.9 | $Zn_3$–$S_{25}$–$Zn_1$ | 106.4 | $S_{61}$–$Zn_4$–$S_{60}$ | 129.9 | $Zn_4$–$S_{61}$–$Zn_7$ | 115.3 |
| $S_{22}$–$Zn_1$–$S_5$ | 100.2 | $Zn_3$–$S_{16}$–$Zn_2$ | 102.1 | $S_{61}$–$Zn_4$–$S_{58}$ | 104.5 | $Zn_5$–$S_{51}$–$Zn_4$ | 105.6 |
| $S_{22}$–$Zn_1$–$S_7$ | 117.3 | $Zn_2$–$S_7$–$Zn_1$ | 107.4 | $S_{61}$–$Zn_4$–$S_{51}$ | 115.6 | $Zn_5$–$S_{35}$–$Zn_6$ | 104.4 |
| $S_{22}$–$Zn_1$–$S_{25}$ | 108.0 | | | $S_{60}$–$Zn_4$–$S_{58}$ | 112.8 | $Zn_5$–$S_{38}$–$Zn_7$ | 103.2 |
| $S_{25}$–$Zn_1$–$S_7$ | 111.6 | | | $S_{60}$–$Zn_4$–$S_{51}$ | 91.3 | $Zn_6$–$S_{45}$–$Zn_7$ | 102.4 |
| $S_{25}$–$Zn_1$–$S_5$ | 126.6 | | | $S_{58}$–$Zn_4$–$S_{51}$ | 98.2 | | |
| $S_7$–$Zn_2$–$S_{14}$ | 108.2 | | | $S_{35}$–$Zn_5$–$S_{37}$ | 131.5 | | |
| $S_7$–$Zn_2$–$S_{16}$ | 101.9 | | | $S_{35}$–$Zn_5$–$S_{51}$ | 104.0 | | |
| $S_7$–$Zn_2$–$S_{27}$ | 111.3 | | | $S_{35}$–$Zn_5$–$S_{38}$ | 99.4 | | |
| $S_{14}$–$Zn_2$–$S_{16}$ | 104.9 | | | $S_{37}$–$Zn_5$–$S_{51}$ | 95.7 | | |
| $S_{14}$–$Zn_2$–$S_{27}$ | 107.8 | | | $S_{37}$–$Zn_5$–$S_{38}$ | 103.2 | | |
| $S_{16}$–$Zn_2$–$S_{27}$ | 122.0 | | | $S_{51}$–$Zn_5$–$S_{38}$ | 126.9 | | |
| $S_{16}$–$Zn_3$–$S_{20}$ | 109.3 | | | $S_{49}$–$Zn_6$–$S_{45}$ | 116.2 | | |
| $S_{16}$–$Zn_3$–$S_{25}$ | 108.7 | | | $S_{49}$–$Zn_6$–$S_{35}$ | 109.9 | | |
| $S_{16}$–$Zn_3$–$S_{30}$ | 115.5 | | | $S_{49}$–$Zn_6$–$S_{34}$ | 101.3 | | |
| $S_{20}$–$Zn_3$–$S_{25}$ | 93.6 | | | $S_{45}$–$Zn_6$–$S_{35}$ | 123.2 | | |
| $S_{20}$–$Zn_3$–$S_{30}$ | 103.3 | | | $S_{45}$–$Zn_6$–$S_{34}$ | 92.0 | | |
| $S_{25}$–$Zn_3$–$S_{30}$ | 123.0 | | | $S_{35}$–$Zn_6$–$S_{34}$ | 109.9 | | |
| | | | | $S_{38}$–$Zn_7$–$S_{42}$ | 97.4 | | |
| | | | | $S_{38}$–$Zn_7$–$S_{45}$ | 108.1 | | |
| | | | | $S_{38}$–$Zn_7$–$S_{61}$ | 105.3 | | |
| | | | | $S_{42}$–$Zn_7$–$S_{45}$ | 104.1 | | |
| | | | | $S_{42}$–$Zn_7$–$S_{61}$ | 111.3 | | |
| | | | | $S_{45}$–$Zn_7$–$S_{61}$ | 126.9 | | |
| Mean value | 109.1±9.3 | Mean value | 105.3±2.8 | Mean value | 109.2±11.8 | Mean value | 106.2±4.7 |

Mean value of S–Zn–S angles in β and α domains: 109.2±1.7°.
Mean of bridging Zn–S–Zn angles in β and α domains: 105.7±3.7°.

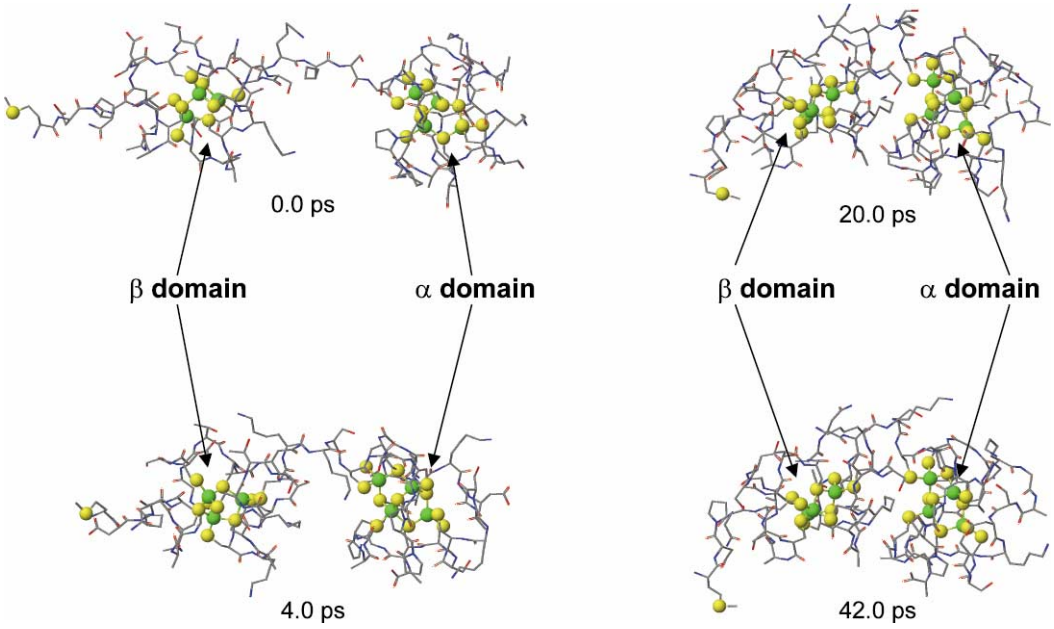


Fig. 13. Conformers extracted from the MD trajectory carried out for rabbit liver $Zn_7$–MT2A at specified time intervals of 0, 4, 20, and 42 ps with a simulated temperature of 300 K. Rabbit liver $Zn_7$–MT2A residues depicted in ball and stick form and color-coded by atom. The four snap-shots show that over 42 ps at 300 K the two domains swing together and become meshed. Atom legend: green = Zn(II), yellow = S, gray = C, blue = N, red = O (reproduced with permission from Huang et al. [65]).

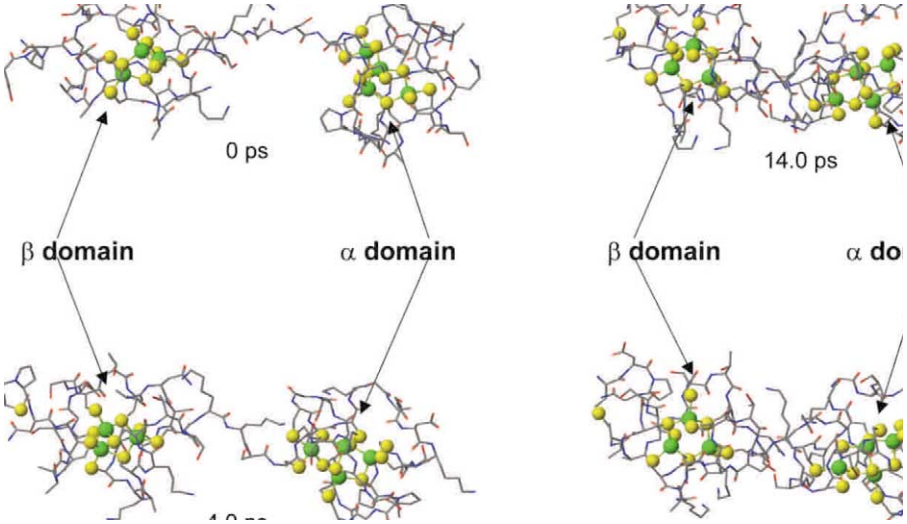


Fig. 14. Conformers extracted from the MD trajectory for rabbit liver $Cd_7$–MT2A at specified time intervals of 0, 4, 14, and 22 ps with simulated temperature of 300 K. Rabbit liver $Cd_7$–MT2A residues depicted in ball and stick form and color-coded by atom. In comparison to $Zn_7$–MT2A (Fig. 11). The four snap-shots show over 22 ps at 300 K the two Cd-domains becoming horizontally compacted. Atom legend: green = Cd(II), yellow = S, gray = C, blue = N, red = O (reproduced with permission from Huang et al. [65]).

domains moved toward each other to form a stable folded structure at about 25 ps (refer to Fig. 14). The difference between rabbit liver $Zn_7$–MT2A and $Cd_7$–MT2A in the stable, folded state was obtained from their MD trajectories. The stable folded 3D structure of rabbit liver $Zn_7$–MT2A formed a 'loop' between two domains, which is accessible by solvent molecules, but this was not observed in the simulation of the rabbit liver $Cd_7$–MT2A (refer to Fig. 13). This could be the explanation by the difference in bond lengths between Zn(II)- and Cd(II)-containing species.

## Acknowledgements

The authors would like to thank the past members of the group whose work has been described in publications referred to here, and their collaborators, Dr. Peter Kille at Cardiff, UK, Professor Peter Norton at UWO, and Professor Michael Siu at York U. We would like to thank Colleen Trevithick, Don Thomas, and Justin Norris for help in many aspects of the work described here. We thank Professor Lars Konermann for use of the mass spectrometer and David Gallagher at CAChe, Fujitsu America for providing the latest CACHE software for MM2, MD, ZINDO, and DFT calculations. We acknowledge financial support from NSERC in the form of equipment and operating funds, NATO for travel funds (to M.J.S. and P.K.), CFI funds for the mass spectrometer (to L.K.), and support by the Academic Development Fund at the UWO (to M.J.S.).

## References

[1] G. Zubay (Ed.), Biochemistry, 4th ed., Brown Publishers/McGraw-Hill, USA, 1998, p. 112.
[2] D. Voet, J.G. Voet, C.W. Pratt (Eds.), Fundamentals of Biochemistry, Wiley, New York, 1999, p. 151.
[3] P.J. Kraulis, A.R.C. Raine, P.L. Gadhavi, E.D. Laue, Nature 356 (1992) 448.
[4] N.P. Pavletich, C.O. Pabo, Science 261 (1993) 1701.
[5] M.J. Stillman, A. Presta, in: R.K. Zalups, J. Koropatnick (Eds.), Molecular Biology and Toxicology of Metals, Taylor & Francis, London, 2000, pp. 1–33.
[6] B.A. Averill, in: L. Que, Jr. (Ed.), Metal Clusters in Proteins (Chapter 13), ACS Books, Washington, DC, 1988, p. 259.
[7] D. Voet, J.G. Voet, C.W. Pratt (Eds.), Fundamentals of Biochemistry, Wiley, New York, 1999, p. 295.
[8] E.I. Stiefel, in: E.I. Stiefel, M. Kazuko (Eds.), Transition Metal Sulfur Chemistry, ACS Books, 1996, pp. 2–3, 117.
[9] B.L. Vallee, in: J.H.R. Kagi, M. Nordberg (Eds.), Metallothionein, Birkhauser Verlag, Basel, 1979, pp. 31–36.
[10] J.H.R. Kagi, Y. Kojima, in: J.H.R. Kagi, Y. Kojima (Eds.), Metallothionein II, Birkhauser Verlag, Basel, 1987, pp. 33–38.
[11] J.F. Riordan, in: J.F. Riordan, B.L. Vallee (Eds.), Metallobiochemistry, Part B, vol. 205, Academic Press, New York, 1991.
[12] M.J. Stillman, in: M.J. Stillman, C.F. Shaw, III, K.T. Suzuki (Eds.), Metallothioneins, VCH Publishers, New York, 1992, pp. 55–127.
[13] J.H.R. Kagi, in: K.T. Suzuki, N. Imura, M. Kimura (Eds.), Metallothionein III, Birkhauser Verlag, Basel, 1993, pp. 32–38.
[14] M.J. Stillman, Coord. Chem. Rev. 144 (1995) 46.
[15] M.J. Stillman, in: N.D. Hadjiliads (Ed.), Cytotoxic, Mutagenic and Carcinogenic Potential of Heavy Metals Related to Human Environment, Kluwer Academic Publishers, The Netherlands, 1997, pp. 139–194.
[16] J.H.R. Kagi, A. Schaffer, Biochemistry 27 (1988) 8509.
[17] M. Margoshes, B.L. Vallee, J. Am. Chem. Soc. 79 (1957) 4813.
[18] M.J. Stillman, C.F. Shaw, III, K.T. Suzuki, in: M.J. Stillman, C.F. Shaw, III, K.T. Suzuki (Eds.), Metallothioneins, VCH Publishers, New York, 1992, p. 1.

[19] P.E. Hunziker, J.H.R. Kagi, in: P.M. Harrison (Ed.), Metallothionein, Part 2, The Macmillan Press, London, 1985, pp. 149–181.
[20] F. Arnesano, L. Banci, I. Bertini, D.L. Huffman, T.V. O'Halloran, Biochemistry 40 (2001) 1528.
[21] S. Helmut (Ed.), Metal Ions in Biological Systems: Concepts of Metal Ion Toxicity, vol. 20, Dekker, New York, 1986, p. 68.
[22] M.H. Bhattacharyya, A.K. Wilson, S.S. Rajan, M. Jonah, in: R.K. Zalups, J. Koropatnick (Eds.), Molecular Biology and Toxicology of Metals, Taylor & Francis, London, 2000, p. 34.
[23] M.P. Waalkes, R. Perez-Olle, in: R.K. Zalups, J. Koropatnick (Eds.), Molecular Biology and Toxicology of Metals, Taylor & Francis, London, 2000, p. 414.
[24] N.O. Narley, J.V. Frei, M.G. Cherian, Lab. Invest. 57 (1987) 397.
[25] M.J. Stillman, in: M.J. Stillman, C.F. Shaw, K.T. Suzuki (Eds.), Metallothioneins, VCH Publishers, New York, 1992, p. 55.
[26] D.H. Winge, C.T. Dameron, in: K.T. Suzuki, N. Imuraand, M. Kimura (Eds.), Metallothionein III, Birkhauser Verlag, Basel, 1993, p. 381.
[27] D.A. Fowle, M.J. Stillman, J. Biomol. Struct. Dyn. 14 (1997) 393–406.
[28] P.A. Presta, D.A. Fowle, M.J. Stillman, J. Chem. Soc. Dalton Trans. (1997) 977.
[29] P. Faller, M. Vašák, Biochemistry 36 (1997) 13341.
[30] M. Vašák, R. Bogumil, in: N.D. Hadjiliads (Ed.), Cytotoxic, Mutagenic and Carcinogenic Potential of Heavy Metals Related to Human Environment, Kluwer Academic Publishers, The Netherlands, 1997, pp. 195–215.
[31] J.H.R. Kagi, in: K.T. Suzuki, N. Imura, M. Kimura (Eds.), Metallothionein III, Birkhauser Verlag, Basel, 1993, p. 29.
[32] J.D. Otvos, I.M. Armitage, Proc. Natl. Acad. Sci. USA 77 (1980) 7094.
[33] J.D. Otvos, R.W. Olafson, I.M. Armitage, J. Biol. Chem. 257 (1982) 2427.
[34] A.H. Robbins, C.D. Stout, in: M.J. Stillman, C.F. Shaw, III, K.T. Suzuki (Eds.), Metallothioneins, VCH Publishers, New York, 1992, p. 31.
[35] A.H. Robbins, D.E. McRee, M. Williamson, S.A. Collett, N.H. Xuong, W.F. Furey, B.C. Wang, C.D. Stout, J. Mol. Biol. 221 (1991) 1269.
[36] W. Braun, M. Vasak, A.H. Robbins, C.D. Stout, G. Wagner, J.H.R. Kagi, K. Wuthrich, Proc. Natl. Acad. Sci. USA 89 (1992) 10124.
[37] W. Lu, M. Kasrai, G.M. Bancroft, M.J. Stillman, K.H. Tan, Inorg. Chem. 29 (1990) 2561.
[38] Z. Gui, A.R. Green, M. Kasrai, M.G. Bancroft, M.J. Stillman, Inorg. Chem. 35 (1996) 6520.
[39] D.T. Jiang, Z.Q. Gui, S.M. Heald, T.K. Sham, M.J. Stillman, Physica B 208/209 (1995) 729.
[40] D.T. Jiang, S.M. Heald, T.K. Sham, M.J. Stillman, J. Am. Chem. Soc. 116 (1994) 11004.
[41] G. Charis, J. Yon, (Eds.), Protein Folding, Academic Press, New York, NY, 1982, pp. 7–350.
[42] Y. Kojima, P.-A. Binz, J.H.R. Kagi, in: C.D. Klaassen (Ed.), Metallothionein IV, Kansas City, USA, 1991, pp. 3.
[43] G.W. Stuart, P.F. Searle, R.D. Palmiter, Nature 317 (1985) 828.
[44] M.J. Stillman, W. Cai, A.J. Zelazowski, J. Biol. Chem. 262 (1987) 4538.
[45] M.J. Stillman, A.J. Zelazowski, J. Biol. Chem. 263 (1988) 6128.
[46] W. Cai, M.J. Stillman, Inorg. Chim. Acta 152 (1988) 111.
[47] Z. Gasyna, A.J. Zelazowski, A.R. Green, E. Ough, M.J. Stillman, Inorg. Chim. Acta 153 (1988) 115.
[48] M.J. Stillman, A.J. Zelazowski, Z. Gasyna, FEBS Lett. 240 (1988) 159.
[49] W. Cai, M.J. Stillman, J. Am. Chem. Soc. 110 (1988) 7872.
[50] M.J. Stillman, A.J. Zelazowski, J. Szymanska, Z. Gasyna, Inorg. Chim. Acta 161 (1989) 275.
[51] M.J. Stillman, A.J. Zelazowski, Biochem. J. 262 (1989) 181.
[52] A.J. Zelazowski, Z. Gasyna, M.J. Stillman, J. Biol. Chem. 264 (1989) 17091.
[53] M.J. Stillman, Z. Gasyna, A.J. Zelazowski, FEBS Lett. 257 (1989) 283.
[54] M.J. Stillman, Z. Gasyna, in: B. Vallee, J.F. Riordan (Eds.), Methods in Enzymology, Metallobiochemistry Part B, Metallothionein and Related Molecules, vol. 205, Academic Press, New York, 1991, p. 540.
[55] A.J. Zelazowski, M.J. Stillman, Inorg. Chem. 31 (1992) 3363.
[56] W. Lu, M.J. Stillman, J. Am. Chem. Soc. 115 (1993) 3291.
[57] W. Lu, A.J. Zelazowski, M.J. Stillman, Inorg. Chem. 32 (1993) 919.
[58] P.A. Presta, M.J. Stillman, Chirality 6 (1994) 521.
[59] M.J. Stillman, P.A. Presta, Z. Gui, D.T. Jiang, Metal-Based Drugs 1 (1994) 375.
[60] A.R. Green, M.J. Stillman, Inorg. Chim. Acta 226 (1994) 275.
[61] A.R. Green, P.A. Presta, Z. Gasyna, M.J. Stillman, Inorg. Chem. 33 (1994) 4159.
[62] P.A. Presta, A.R. Green, A.J. Zelazowski, M.J. Stillman, Eur. J. Biochem. 227 (1995) 226.
[63] A.R. Green, M.J. Stillman, Inorg. Chem. 35 (1996) 2799.
[64] P.A. Presta, M.J. Stillman, J. Inorg. Biochem. 66 (1996) 231.
[65] Z. Huang, J. Chan, J. Norris, M.E. Merrifield, P. Kille, M.J. Stillman (2002), submitted for publication.
[66] M.J. Stillman, D. Thomas, C. Trevithick, X. Guo, M. Siu, J. Inorg. Chem. 79 (2000) 11.
[67] P.A. Presta, A.R. Green, M.J. Stillman (2002), submitted for publication.
[68] Y.J.C. Le Blanc, P.A. Presta, J. Veinot, D. Gibson, K.W.M. Siu, M.J. Stillman, Protein Pept. Lett. 4 (1997) 313.
[69] M.E. Merrifield, Z. Huang, P. Kille, M.J. Stillman, J. Inorg. Biochem. 88 (2002) 144.
[70] J.B. Fenn, M. Man, C.K. Meng, S.K. Wong, C.M. Whitehouse, Science 246 (1989) 46.
[71] H.E. Whitowska, C.H.L. Shackleton, K. Dahlman-Whight, J.Y. Kim, J.A. Gustafsson, J. Am. Chem. Soc. 117 (1995) 3320.
[72] R.H. Griftey, K.A. Sannes-Lowery, J.J. Drader, V. Mohan, E.E. Swayze, S.A. Hostadler, J. Am. Chem. Soc. 122 (2000) 9933.
[73] X. Yu, M. Wojciechowski, C. Fenselau, Anal. Chem. 65 (1993) 1355.
[74] J.A. Loo, R.R.O. Loo, in: R.B. Cole (Ed.), Electrospray Ionization Mass Spectrometry (Chapter 11), Wiley, New York, 1997, pp. 385–419.
[75] K.J. Laidler (Ed.), Reaction Kinetics: Homogeneous Gas Reactions, vol. 1, Pergamon Press, London, UK, 1963, p. 1.
[76] M.T. Salgado, C. Trevithick, M.J. Stillman (2002), submitted for publication.
[77] R. Wiesendanger, in: R. Wiesendanger (Ed.), Scanning Probe Microscopy, Analytical Methods, Springer, Berlin, 1998, p. 1.
[78] D. Bonnell, B.D. Huey, in: D. Bonnell (Ed.), Scanning Probe Microscopy and Spectroscopy, Theory, Techniques, and Applications, 2nd ed., Wiley-VCH, 2001, p. 10.
[79] T.P. Beebe, T.E. Wilson, D.F. Ogletree, J.E. Katz, R. Balhorn, M.B. Salmeron, W.J. Siekhaus, Science 243 (1989) 370.
[80] G. Lee, P.G. Arscott, V.A. Bloomfield, D.F. Evans, Science 244 (1989) 475.
[81] M. Parker, M.C. Davies, S.J.B. Tendler, J. Phys. Chem. 99 (1995) 16155.
[82] R.D. Edstrom, M.H. Meinke, X. Yang, R. Yang, D.F. Evans, Biochemistry 28 (1989) 4939.
[83] J. Zhang, Q. Chi, S. Dong, E. Wang, J. Chem. Soc. Faraday Trans. 91 (1995) 1471.

[84] B. Zhang, E. Wang, J. Chem. Soc. Faraday Trans. 93 (1997) 327.
[85] J.J. Davis, C.M. Halliwell, H.A.O. Hill, G.W. Canters, M.C. van Amsterdam, M.P. Verbeet, New J. Chem. 10 (1998) 1119.
[86] J.J. Davis, H.A.O. Hill, A. Kurz, C. Jacob, W. Maret, B.L. Vallee, Phys. Chem. Commun. 1 (1998) 12.
[87] J. Chan, P.R. Norton, M.J. Stillman (2002), submitted for publication.
[88] M. Boncheva, H. Vogel, Biophys. J. 73 (1997) 1056.
[89] M.H. Frey, G. Wagner, M. Vašák, O.W. Sãrensen, D. Neuhaus, E. Wörgrötter, J.H.R. Kägi, R.E. Ernst, K. Wüthrich, J. Am. Chem. Soc. 107 (1985) 6847.
[90] W. Braun, G. Wagner, E. Wörgrötter, M. Vašák, J.H.R. Kägi, K. Wüthrich, J. Mol. Biol. 187 (1986) 125.
[91] M. Good, R. Hollenstein, P.J. Sadler, M. Vašák, Biochemistry 27 (1988) 7153.
[92] R.W. Briggs, I.M. Armitage, J. Biol. Chem. 257 (1982) 1259.
[93] C.W. Peterson, S.S. Narula, I.M. Armitage, FEBS Lett. 397 (1996) 85.
[94] A. Arseniev, P. Schultze, E. Wörgrötter, W. Braun, G. Wagner, M. Vašák, J.H.R. Kägi, K. Wüthrich, J. Mol. Biol. 201 (1988) 637.
[95] B.A. Messerle, A. Schaffer, M. Vašák, J.H.R. Kägi, K. Wüthrich, J. Mol. Biol. 225 (1992) 433.
[96] CACHE, PC version 4.5, 5.0. CACHE Scientific, Fujitsu America.
[97] N.L. Allinger, J. Am. Chem. Soc. 99 (1977) 8127.
[98] J.L. Hencher, M.A. Khan, F.F. Said, D.G. Tuck, Polyhedron 4 (1985) 1263.
[99] K.S. Hagen, R.H. Holm, Inorg. Chem. 22 (1983) 3171.
[100] Z. Huang, J. Mackie, M.J. Stillman (2002), submitted for publication.